



Analysis of a High-Power, Resonant DC-DC converter for DC Wind Turbines

Dincan, Catalin Gabriel; Kjær, Philip Carne; Chen, Yu-Hsing; Munk-Nielsen, Stig; Bak, Claus Leth

Published in:
I E E Transactions on Power Electronics

DOI (link to publication from Publisher):
[10.1109/TPEL.2017.2770322](https://doi.org/10.1109/TPEL.2017.2770322)

Publication date:
2018

Document Version
Accepted author manuscript, peer reviewed version

[Link to publication from Aalborg University](#)

Citation for published version (APA):
Dincan, C. G., Kjær, P. C., Chen, Y.-H., Munk-Nielsen, S., & Bak, C. L. (2018). Analysis of a High-Power, Resonant DC-DC converter for DC Wind Turbines. *I E E Transactions on Power Electronics*, 33(9), 7438-7454. <https://doi.org/10.1109/TPEL.2017.2770322>

General rights

Copyright and moral rights for the publications made accessible in the public portal are retained by the authors and/or other copyright owners and it is a condition of accessing publications that users recognise and abide by the legal requirements associated with these rights.

- Users may download and print one copy of any publication from the public portal for the purpose of private study or research.
- You may not further distribute the material or use it for any profit-making activity or commercial gain
- You may freely distribute the URL identifying the publication in the public portal -

Take down policy

If you believe that this document breaches copyright please contact us at vbn@aub.aau.dk providing details, and we will remove access to the work immediately and investigate your claim.

Analysis of a high power, resonant DC-DC converter for DC wind turbines

Catalin Dincan, *Student Member, IEEE*, Philip Kjaer, *Senior Member, IEEE*, Yu-hsing Chen, Stig Munk-Nielsen, Claus Leth Bak, *Senior Member, IEEE*,

Abstract—This paper is introducing a new method of operation for a series resonant converter, with intended application in megawatt high-voltage DC wind turbines. Compared to a frequency controlled series resonant converter operated in sub resonant mode, the method (entitled pulse removal technique) allows the design of the medium frequency transformer for highest switching frequency, while being operated at lower frequency without saturation. The main focus of this paper is to identify and analyse the operating modes of the converter with pulse removal technique. With the use of variable frequency and variable phase displacement in sub resonant mode, the new method of operation promises transformer size reduction and facilitates soft-switching transition of the IGBTs and line frequency diodes on rectifier side. Four modes of operation are identified, while equations for output power, voltage and current stress are identified. Experimental results are concluded on a 1 kW, 250V / 500V prototype.

Index Terms—resonant converter, medium voltage DC, medium frequency transformer, offshore wind farm, high voltage converter

NOMENCLATURE

CCM	Continuous conduction mode.
DCM	Discontinuous conduction mode.
$HVDC$	High voltage direct current.
$LVDC$	Low voltage direct current.
$MVDC$	Medium voltage direct current.
SRC	Series resonant converter.
$SRC\#$	Series resonant converter "sharp".
C_r	Resonant (tank) capacitor.
δ	Inverter legs phase displacement.
F_{sw}	Switching frequency.
F_r	Resonant frequency.
M	Voltage gain.
N	Transformer turns ratio
i_m	Transformer magnetizing current.
i_{out}	Output current of the converter.
i_{rp}	Primary resonant current.
i_{rs}	Secondary resonant current.
i_r	Rectified current
K	Constant.
L_r	Resonant (tank) inductor.
L_m	Transformer magnetizing inductance.
P_{in}	Input power.
P_{out}	Output power.
Q	Converter quality factor.
q_s	Resonant capacitor stored charge.

V_{in}	Input voltage.
V_{out}	Output voltage.
V_g	Inverter output voltage.
V'_g	Inverter reflected voltage on secondary.
V_o	Rectifier voltage.
V'_o	Rectifier voltage reflected on primary.
V_{Cr}	Resonant capacitor voltage.
V_t	Resonant tank voltage
ΔV	Voltage difference between V'_g and V_o .
T_{sw}	Switching period.
T_r	Resonant current pulse period.
T_{rec}	Rectifier diode reverse recovery time.
ω_r	Resonant angular frequency.
ω_{sw}	Switching angular frequency.
γ	Normalized switching frequency.
Z_c	Resonant tank characteristic impedance

I. INTRODUCTION

PRESENT offshore wind farms use mainly HVAC collection grids to transmit the energy collected from wind turbines to onshore, while other solutions use HVAC up to a large rectifier and then to the mainland through a high voltage DC (HVDC) transmission line. According to [1]-[4], HVDC wind farms could operate with higher efficiency when connected to a MVDC (Medium Voltage Direct Current) collection grid. A single line diagram for the DC wind farm is shown in Fig. 1a. The motivation lays in the fact that the levelized cost of energy (LCOE) could be reduced by as much as 3%, by improving the efficiency with 2% and reducing the bill of materials (BoM) costs by at least 1% [1]. It is expected in the near future, that MVDC grids will be the preferred solution for energy distribution and collection grids.

A desired, but challenging component of such a system would be the MV DC/DC converter located in the wind turbines. A good candidate solution, with more benefits than deficits, could be a unidirectional series resonant converter (SRC). The proposed topology is composed of: low voltage (LV) inverter, one monolithic transformer (with one primary and secondary winding) and a medium voltage (MV) rectifier built with series connected diodes. The topology will be referred as SRC# and it's shown in Fig. 1b, with the ratings from Table I.

High availability, efficiency and power density are targets for the DC/DC converter and they can be achieved through the use of series resonant converter. Considering the high voltage specifications, a transformer with high turns ratio

All authors are with the Department of Energy Technology, Aalborg University, Aalborg, Denmark. Email: cgd@et.aau.dk

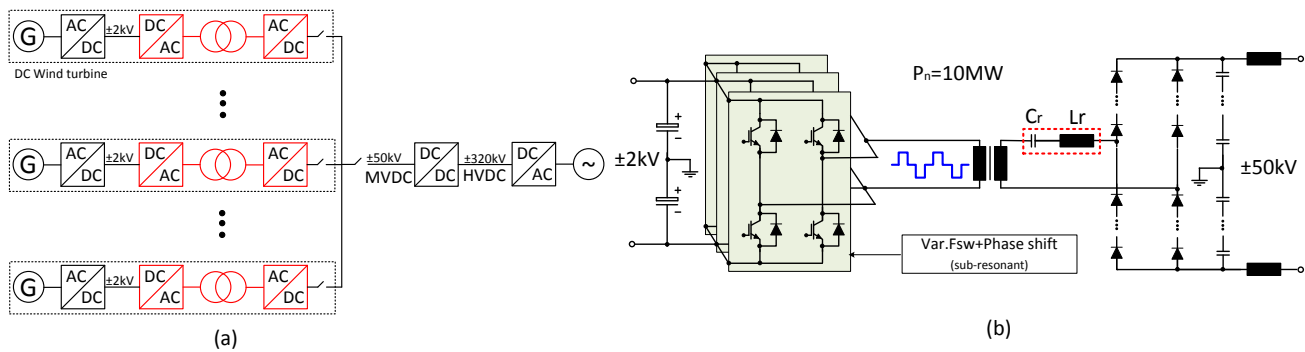


Fig. 1. (a) Single line diagram of DC wind farm; (b) Series resonant converter with new method of operation (SRC#).

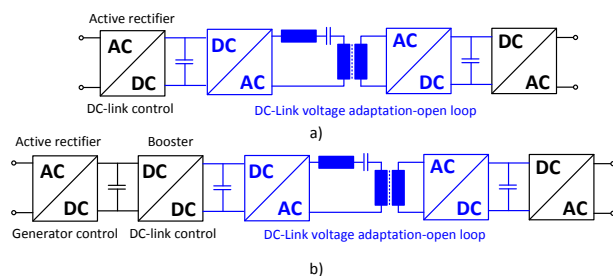


Fig. 2. Turbine converter with SRC operated in sub-resonant mode at constant frequency in open loop (a); Concept with DC/DC converter operated at resonant mode and constant frequency in open loop (b).

TABLE I
RATINGS FOR SRC#

Parameter	Value
Nominal power, P_n	10 MW
Nominal input voltage V_{in}	± 2 kV
Nominal output voltage V_{out}	± 50 kV
Isolation level	± 75 kV
Inverter	4x3 in parallel IGBT(6500V-x-750A)
Rectifier	4x40 in series diode (6500V-x-750A)
Frequency range F_{sw}	0-1000 Hz
Resonant capacitor C_r	0.250 μ F
Resonant inductor L_r	78 mH
Magnetizing inductance L_m	10 mH
Transformer core weight F_e	800 kg
Transformer winding weight C_u	340 kg
Resonant capacitor energy E_{cap}	1250 J
Resonant inductor energy E_{ind}	1250 J

should be employed. But, high voltage transformers suffer from the impact of leakage inductance, which can lead to high overshoots across the switching semiconductors. Through the use of a series resonant tank, the leakage inductance can now be incorporated in the tank and actually help reducing losses. For high power operation, the topology has been investigated mainly in traction applications [5]-[9] and in solid-state transformer [10]-[12]. Operated at constant frequency and in sub-resonant mode it is known as half cycle discontinuous-conduction-mode series-resonant converter (HC-DCM-SRC). For these particular applications, the converter couples two DC link voltages with a fixed voltage transfer ratio, but has no control possibilities (cf. Fig.2a).

For a wind turbine on the other hand, the DC/DC converter must have the functionality of controlling the LV DC bus voltage, while offering galvanic separation and a high voltage gain. A candidate solution (cf. Fig. 2b) was proposed in [13] and it employs a SRC, operated at resonant mode and with constant frequency, while a front end boost converter controls the input DC-link, increasing thus number of components, complexity and losses.

In [26], a per-phase configuration of the series resonant converter is proposed, with three single phase rectifier series-connected on the output. The topology is controlled through variable duty cycle and constant frequency, while being operated exclusively in super-resonant mode. The drawback of this mode are hard turn-off losses on both inverter and rectifier side

switches. No efficiency analysis or measurement was reported and the circuit would appear to suffer from technical barriers on implementing 2-3 MVA, 10-kHz monolithic transformers. Non-isolated topologies have also been proposed in prior art: [27] and [28] propose a single and three phase topology, while employing low-cost thyristors. The topology is similar to a parallel resonant converter, but suffers from high voltage stress across the semiconductors and resonant tank. In a DC wind turbine application, galvanic separation is preferred for protection and safety reasons, by effectively decoupling the generator and its rectifier from that of the dc/dc converter.

In order to control the LV DC bus voltage, our work proposes a method of operation for the SRC, where variable frequency and phase shift control in sub-resonant mode are applied. The benefits and deficits of the method are discussed and compared to a SRC operated only with frequency control. The paper deals with the review of classic SRC and motivates the need for pulse removal technique, in order to avoid a bulky transformer. Four modes of operation are identified and analysed, while experiment results from a 1 kW, 500V setup are used to validate the expected behaviour.

The paper is organized as follows: in Section II, modes of operation for the classic SRC are reviewed and preferred mode of operation for a high power converter is selected. In Section III, operation principle of the SRC# is introduced and an explanation of why it's efficient with tank on rectifier side is presented. Section IV provides analysis of SRC# modes

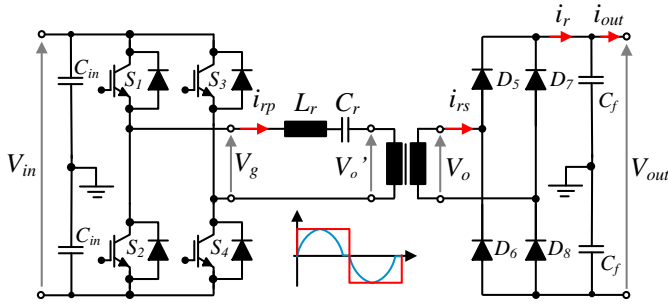


Fig. 3. Series resonant converter (SRC).

of operation, while in Section V, simulation results of steady state operation with the target converter are shown. In Section VI, output power, voltage and current stress characteristics are identified. Section VII provides the experiment results from a 1 kW prototype, confirming SRC# expected behaviour and Section VIII concludes on the results.

II. REVIEW OF SERIES RESONANT CONVERTER

A. Theory of operation

In order to fully comprehend pulse removal technique, a review of series resonant converter modes of operation and control is necessary. Therefore, consider the first SRC design, with tank on inverter side, as shown in Fig. 3, where initially the transformer magnetizing inductance L_m is not considered. When the two complementary switching pairs (S1, S2) and (S3, S4) are opened and closed alternately, a square wave voltage V_g of defined frequency F_{sw} and duty cycle D is applied to the resonant LC tank while the rectifying bridge is left uncontrolled, i.e only diodes are in operation. The resonant frequency F_r , resonant angular frequency ω_r and characteristic impedance of the tank are further defined in eq. (1), (2) and (3). V_g induces a resonant current i_{rp} in the tank circuit, which when rectified and filtered is fed into the output voltage network. The magnitude and shape of the output current is determined by the ratio between F_{sw} and F_r . This explanation is valid for all modes of operation [14]-[16].

$$F_r = \frac{1}{2\pi\sqrt{L_r C_r}} \quad (1)$$

$$\omega_r = 2\pi F_r \quad (2)$$

$$Z_c = \sqrt{\frac{L_r}{C_r}} \quad (3)$$

B. Possible modes of operation

For a SRC, three modes of operation are possible: sub-resonant mode (Fig. 4a and Fig 4b), resonant mode (Fig. 4c) and super-resonant mode (Fig. 4d). In sub-resonant mode, F_{sw} is lower than F_r , while in super-resonant mode it's higher. In resonant mode F_{sw} is equal to that of the resonant tank, meaning switching occurs exactly at the zero crossing event of the current. For both sub-resonant and super-resonant modes,

TABLE II
SWITCHING CHARACTERISTICS FOR SRC OPERATING MODES

	Switching on	Switching off
Frequency Control Sub-resonant DCM	ZVS	ZCS
Frequency Control Sub-resonant CCM	Hard	ZCS
Frequency Control super-resonant	ZVS	ZCS
Resonant mode	ZVS	ZCS
Phase shift sub-resonant	Hard	Hard
Phase shift super-resonant	ZVS	Hard
Dual control sub-resonant	ZVS	ZVS
Dual control super-resonant	ZVS	Hard

two states of conduction can exist: continuous and discontinuous. Discontinuous conduction mode (DCM-Fig. 4a) for sub-resonant mode is characterized by the presence of zero current sub-interval. In that period, all of the rectifier diodes are reversed biased, until V_g changes sign. Continuous conduction mode (CCM-Fig. 4b) appears when the resonant current rings continuously for the full switching period. Regarding control methods, three different methods are identified in prior art for sub-resonant and super-resonant mode: frequency control (see Fig. 4 a, b, c, d), phase shift control (see Fig. 4 e, f) and dual control (see Fig. 4 g, h). By frequency control of input voltage, the effective resonant tank impedance varies with the switching frequency. The phase-shift method is controlling the applied voltage to the resonant tank by changing the duty cycle of the inverter (square wave) voltage, while having constant switching frequency. It can be applied in super-resonant mode (Fig. 4e) or sub-resonant mode (Fig. 4f). With dual control, a combination of variable frequency and phase-shift is applied in order to control transformer primary voltage and the switching current. Dual control in super resonant mode (Fig. 4h) has been published in prior art [25], while the dual control in sub-resonant mode (Fig. 4g) has not been investigated. Pulse removal technique covers this area. Switching characteristics at turn on and off for frequency, phase shift and dual control are further mentioned in Table II.

C. Selection of mode of operation and control method

The mode of operation and control method for the SRC are in general selected based on the application type. For example, at low power and high voltage, applications prefer to employ super resonant and phase shift control [20]-[24]. A three phase variant of the SRC operated in resonant mode is described in [2] and [18] and promises efficiency above 99% but lacks controllability. On the other hand, constant frequency and sub-resonant mode are applied in traction and solid state applications like [19]. Mode of operation and control method are selected based on inverter side device selection and application requirements. Considering the high power and medium voltage application in this case, 6.5 kV IGBTs will be employed on the inverter side, while 6.5kV line frequency diodes are used on rectifier side. Most of the available publications which use a resonant topology are addressing low power and low voltage applications and are using MOSFETs with switching frequencies in the range of hundreds of kilohertz. For those kind of applications, super-resonant mode is attractive, as it allows ZVS at turn on. But, as

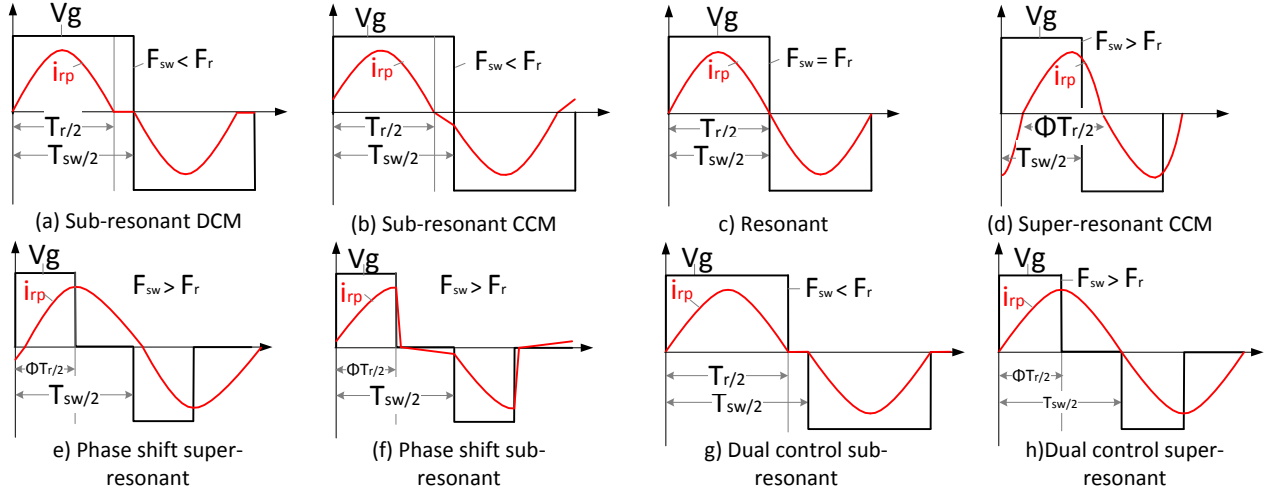


Fig. 4. SRC modes of operation and control methods: frequency control (a,b,c,d); phase shift control (e,f); dual control (g,h).

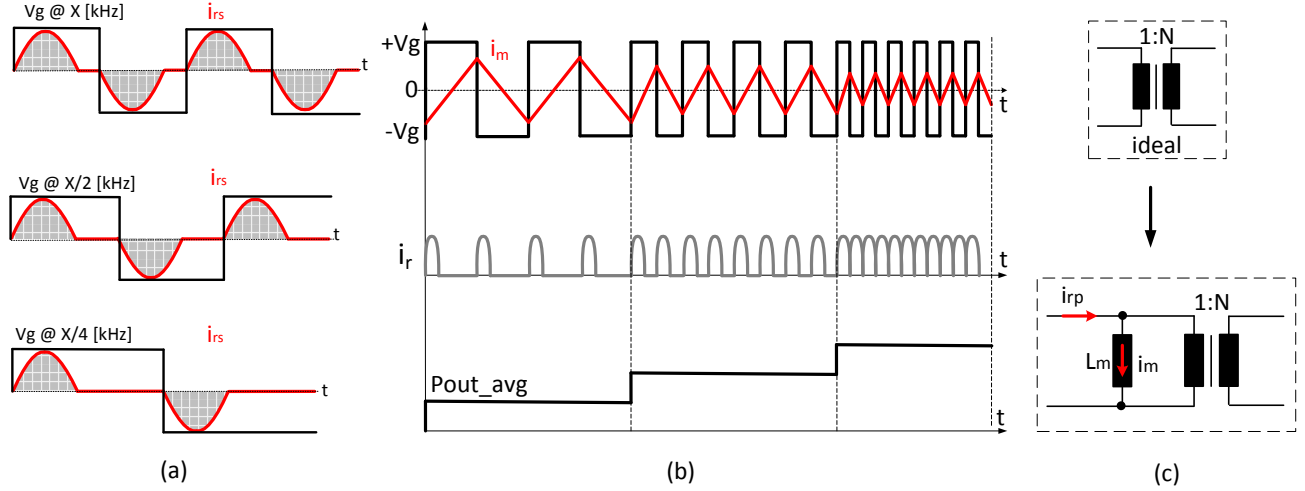


Fig. 5. Frequency control of SRC in sub-resonant DCM: operation with different F_{sw} (a); impact of variable F_{sw} on magnetizing current (b); ideal and non-ideal transformer (c).

also stated in [29], the main contributors to the overall losses with IGBT applications are the turn-OFF losses. According to [30] and [31] the main reason is that these semiconductors are characterized by a bipolar power stage, that, in order to block HV, comprise a considerable large N-base region, which stores a large amount of charge during the conduction phase of the semiconductor. When the switch is turned off, this stored charge is evacuated from the semiconductor, causing tail currents that overlap with the blocking voltage, generating high switching losses. Therefore, a mode of operation that allows ZCS or a small current at turn-off needs to be selected. The obvious mode of operation is therefore sub-resonant mode for IGBT applications. Another particular reason why sub-resonant operation is attractive and with reference to Fig. 5a is that regardless of switching frequency, during every switching period a full resonant pulse is sent to the load. This means if the converter operates in DCM mode, intervals of zero current will appear. Operated below resonant frequency, it

allows the LV and MV side switches to operate with ZCS at turn off. Further on, if frequency control is implemented, output power is dependent on the amount of energy transfer to the output stage, making it a function of number of energy pulses transferred to the output, as seen in Fig. 5b. For an SRC operated in DCM mode, an energy pulse is dependent on the resonant capacitor C_r and its voltage V_{Cr} , as it determines the stored charge q_s , shown in eq. (4), where $V_{Cr} = 2 \cdot V_{in}$.

$$q_s = C_r \cdot (2V_{Cr}) \quad (4)$$

The relation between output averaged current and stored charge is given by eq. (5):

$$i_{out} = \frac{2 \cdot q_s}{t_s} = 2 \cdot q_s \cdot F_{sw} \quad (5)$$

Combining eq. (4) into (5), will give (6):

$$i_{out} = 8 \cdot C_r \cdot F_{sw} \cdot V_{in} \quad (6)$$

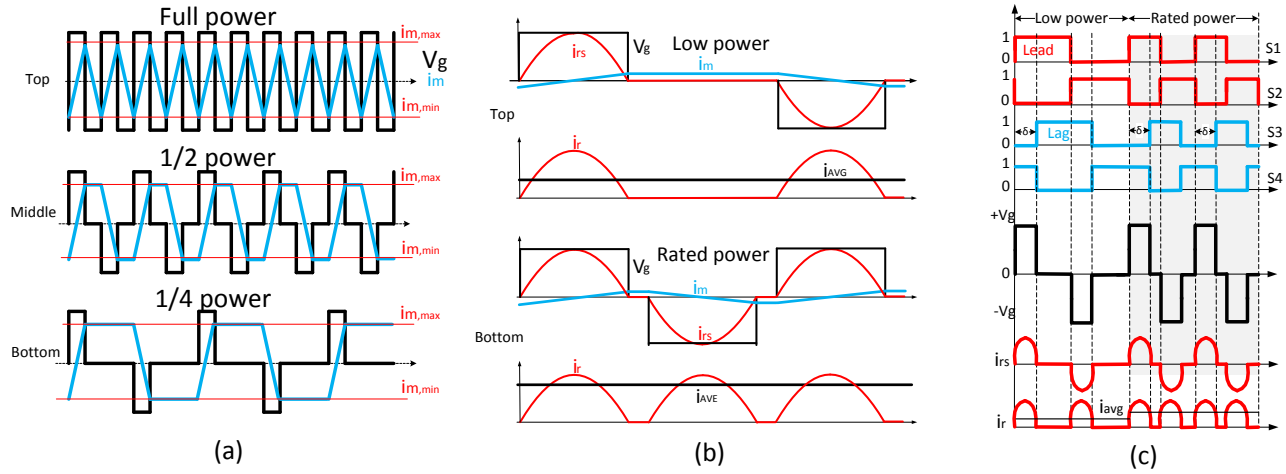


Fig. 6. Pulse removal technique (a); Operation of SRC# at low and high power (b); Switching pattern with variable frequency and phase shift (c)

Considering that $P_{out} = I_{out} \cdot V_{out}$ and $V'_{out} = \frac{V_{out}}{N}$ the previous mentioned relation between output power and switching frequency is determined in (7):

$$P_{out} = \frac{8 \cdot C_r \cdot F_{sw} \cdot V_{in} \cdot V_{out}}{N} \quad (7)$$

Thus, if an SRC should be operated only in DCM mode, eq. (7) provides a simple function, which could be implemented in a feedforward controller. Low frequency operation means low power output, while high frequency operation will deliver a high power output. On the other hand, the disadvantage of operating the SRC with resonant tank on inverter side in sub-resonant mode and frequency control, is that the transformer and output filter now need to be designed for the lowest frequency point and the magnetizing inductance needs therefore to be considered, as seen in Fig. 5c and included in the schematic. Fig. 5b (top) shows how the magnetizing current i_m varies with frequency, being in a direct relation with applied volt-seconds. Below lowest operational frequency, saturation and transformer induced oscillations will occur [32], [33]. A means of avoiding this must be implemented, otherwise, designing medium frequency transformers with SRC operated in sub resonant mode is not possible.

III. OPERATION PRINCIPLE OF THE SRC#

A. Pulse removal technique

Pulse removal technique was initially described in [17] and it's further explained in following paragraphs. As mentioned previously, sub-resonant operation and frequency control are optimal for IGBT applications as they allow soft-switching at turn-off and allow the SRC to control output power. The question is now, how can the transformer be operated with variable frequency and be designed at highest operating frequency, while avoiding saturation at lower frequency. One possible way and with reference to Fig. 6a, is to make V_g a function of square wave pulses, meaning a pulse with determined length is applied to the inverter, but the distance between pulses

varies as a function of output power. As the length of every voltage pulse is fixed, the amplitude of magnetizing current i_m will be constant. Fig. 6a (top) shows the inverter voltage V_g operating at highest frequency, providing the maximum number of voltage pulses per unit time, while i_m varies between a maximum and minimum value. Fig. 6a (middle) and (bottom) indicate that if variable zero voltage periods are inserted between the pulses, i_m will not go above or below maximum and minimum values, but remain constant. Further on and with ref. to Fig. 6b, if the applied voltage V_g has the same length as the resonant pulse i_{rs} , then frequency control in sub-resonant mode becomes possible, allowing the design of the transformer for highest operating point. In particular, Fig. 6b (top) relates to a lower power output (fewer current pulses) than Fig. 6b (bottom), which relates to higher power output. Fig. 6c shows transistors switching pattern, inverter voltage V_g , secondary resonant current i_{rs} and rectifier current i_r , where a pulse removal technique is implemented with a combination of frequency and phase shift control. Another aspect worthy to mention is that, the length of one V_g pulse needs to consider the impact of rectifier diode reverse recovery time T_{rec} , as seen in Fig. 7c.

B. Resonant tank on inverter or rectifier side

Applying pulse removal technique is successful only if the resonant tank is placed on the rectifier side of the transformer, as explained in the following. When LC tank is placed on inverter side, V_g is the inverter voltage and V_o' is the rectifier voltage reflected on inverter side, the main goal is to achieve zero volts on transformer primary winding, as soon as the resonant current reaches zero, thus stopping any flux build-up. Consider the equivalent circuits and corresponding waveforms of SRC with tank on inverter side (Fig. 7a) and with tank on rectifier side (Fig. 7b). In the first case, transformer primary voltage is the rectifier reflected voltage on inverter side, namely V_o' . Looking at principle waveforms from (Fig. 7a (top), it is noticed that even if V_g is clamped to zero during Q1 sub-interval, resonant capacitor voltage V_{Cr} is slowly

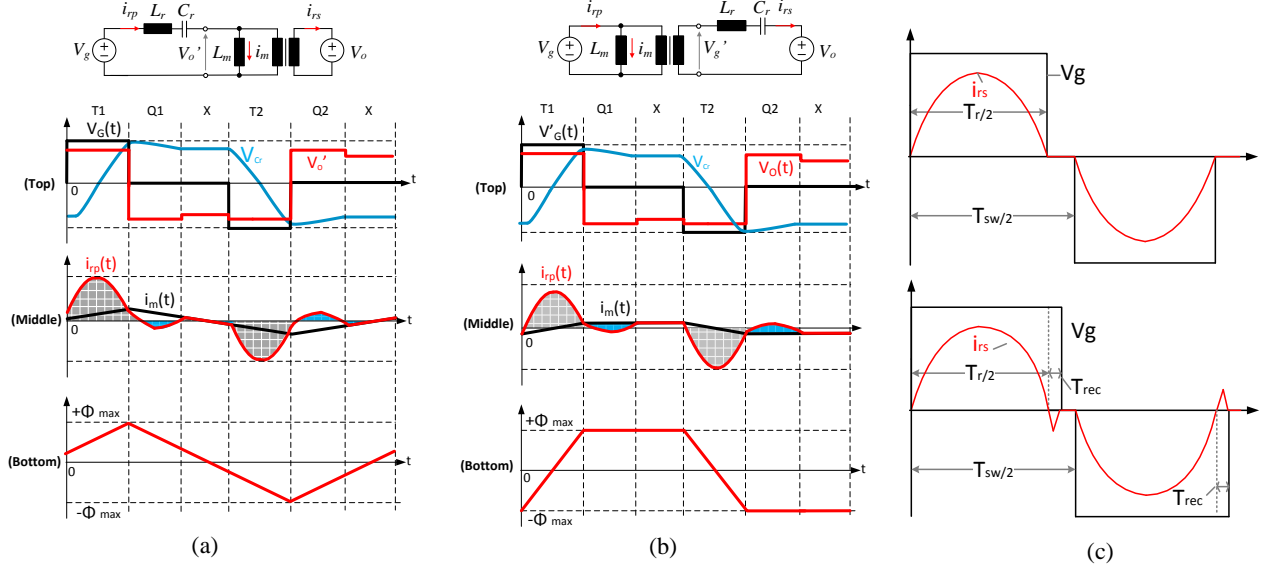


Fig. 7. Characteristic waveforms for SRC# with tank on inverter side (a) and rectifier side (b): top - inverter voltage V_g , rectifier voltage V_o , resonant capacitor voltage V_{cr} ; middle - primary resonant current i_{rp} , magnetizing current i_m ; bottom - magnetic flux Φ ; Impact of rectifier diode reverse recovery on length of V_g voltage pulse (c).

discharged through the magnetizing inductor, not allowing zero volts on the primary. During sub-interval X, transformer primary voltage has the same level as capacitor voltage, but with an opposite sign. In other words, it's not possible to get zero volts on primary winding, even if V_g is zero. Fig. 7a (middle) and (bottom) show primary resonant current i_{rp} , magnetizing current i_m and the magnetic flux Φ , as a function of V_o' and time.

In the second case with LC tank on rectifier side, (see Fig. 7b top), will mean that transformer primary excitation voltage will be controlled directly through V_g , thus limiting the volt-seconds and allowing for lower magnetizing flux, as seen in Fig. 7b (bottom). Comparing the shape of magnetizing current i_m from Fig. 7b (middle) to the one from Fig. 7a (middle), it becomes evident why pulse removal technique is efficient only with the LC tank on rectifier side. The drawback is that the tank needs to be designed for medium voltage levels, impacting insulation, clearance and creepage specifications.

With this arrangement, operating in a sub-resonant mode permits a full resonant cycle of the LC circuit current to pass within a single switching cycle of the full bridge, allowing ZVS at turn-on and a low turn-off current for inverter switches, while the rectifier diodes will experience ZVS at turn-on and ZCS at turn-off.

C. Description of SRC#

The series resonant converter with the new method of operation (SRC#) is depicted in Fig. 8 and comprises a full bridge inverter, monolithic 1:N transformer, resonant tank and medium voltage rectifier. Power flows from V_{in} to V_{out} . The switch pairs (S1/S2) and (S3/S4) as indicated in Fig. 10a, operate at a 50% duty cycle. Determining (S1,S2) as leading leg, will generate Q1 and Q2 sub-intervals (Fig. 10b), while

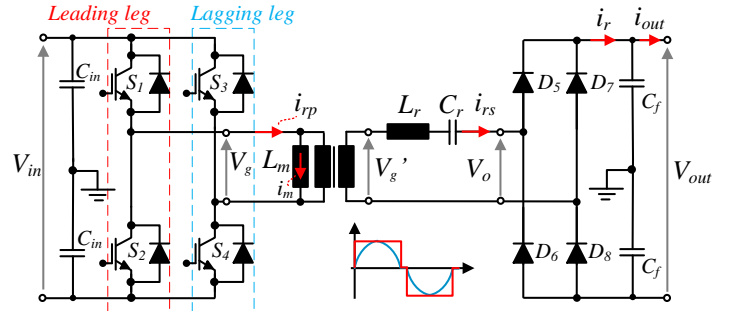


Fig. 8. Series resonant converter with new method of operation: SRC#

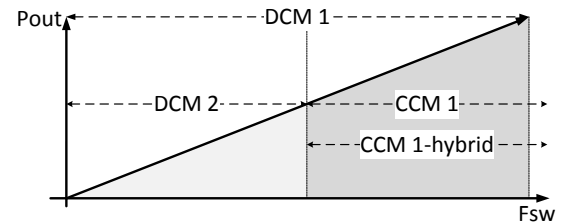


Fig. 9. Power to frequency relationship, for an SRC#

if (S3,S4) is the leading leg, will determine P1 or P2 sub-intervals (Fig. 10c). Q and P sub-intervals are explained later in the paper. For simplicity, in the following paragraphs (S1, S2) is considered the leading leg. Commutation of switches on the leading leg is phase shifted with respect to the conduction of switches on the lagging leg, with a duration δ , equal to a resonant period, resulting in a quasi-square excitation voltage

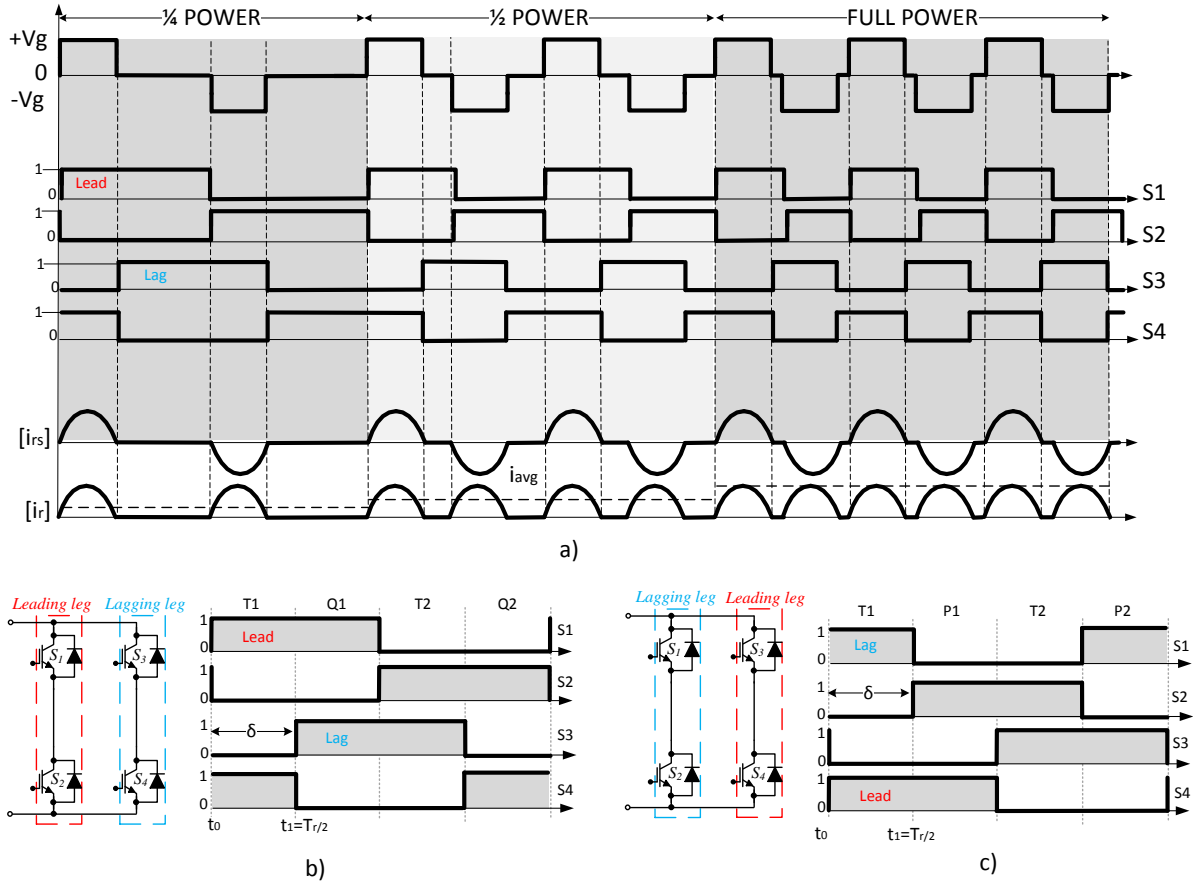


Fig. 10. SRC# switching pattern (a); Switching pattern with (S1,S2) as leading leg (b); Switching pattern as (S3,S4) leading leg (c).

as seen in Fig. 10a. The applied square wave voltage passes through the transformer (V_g referred to rectifier side is V'_g) and excites the tank and a resonant tank current i_{rs} starts to flow. After rectification and filtering it is fed into the medium voltage network, V_{out} . Up to this point there is no operational difference compared to a constant frequency phase shift control, which is normally applied for operation in super resonant mode, to achieve ZVS at turn on. As IGBTs are employed, ZCS or a low current at turn off is necessary, so SRC# operates in sub-resonant mode. The particular case for SRC# is that the implemented phase shift has the same length as the resonant pulse ($T_r/2$), as seen in Fig. 12a. This means that as soon as the secondary resonant current reaches zero, V'_g is switched to zero, i.e. the pulsed voltage is removed. Now, because the converter needs to control output power, just like in the case of frequency control of the classical SRC, also here output power has a linear relation to the number of resonant pulses transferred per second, as depicted in Fig. 9. Therefore, the excitation voltage V_g , becomes a function of frequency and phase shift angle, with operation in sub-resonant mode. This means the zero voltage sub-interval has different lengths for different power levels.

IV. SRC# CONDUCTION MODES

Considering that SRC# is operating in sub resonant mode, four modes of conduction (two discontinuous and two continuous) will appear under steady state operation: DCM1, DCM2, CCM1-hybrid and CCM1. Switching frequency F_{sw} and voltage difference ΔV between inverter voltage reflected on rectifier side V'_g (where $V'_g = V_g \cdot N$) and V_o will determine whether the converter operates in one conduction state or another. A summary of these conditions is shown in Table III. Discontinuous and continuous modes are characterized by the number of half resonant cycles that appear during a half switching period, with the difference that in DCM modes, a period of no conduction appears, while in CCM modes the current never ceases to flow. [14].

DCM1 can occur in the entire operating range (for frequencies from 0 to F_r) during transient states, when the resonant capacitor voltage is increasing or decreasing to certain values. DCM2 can occur only for frequencies below $F_r/2$, as two half resonant cycles followed by no conduction period are not possible above half of F_r . Transition from DCM1 to DCM2 will occur, as soon as $V_{Cr} \geq V_o$, implying energy will flow towards output voltage network. Transition from DCM1 to CCM1-hybrid occurs when $F_{sw} \geq F_r/2$. As ΔV determines peak resonant current and voltage, when $V_{Cr} \geq (V'_g + V_o)$ and

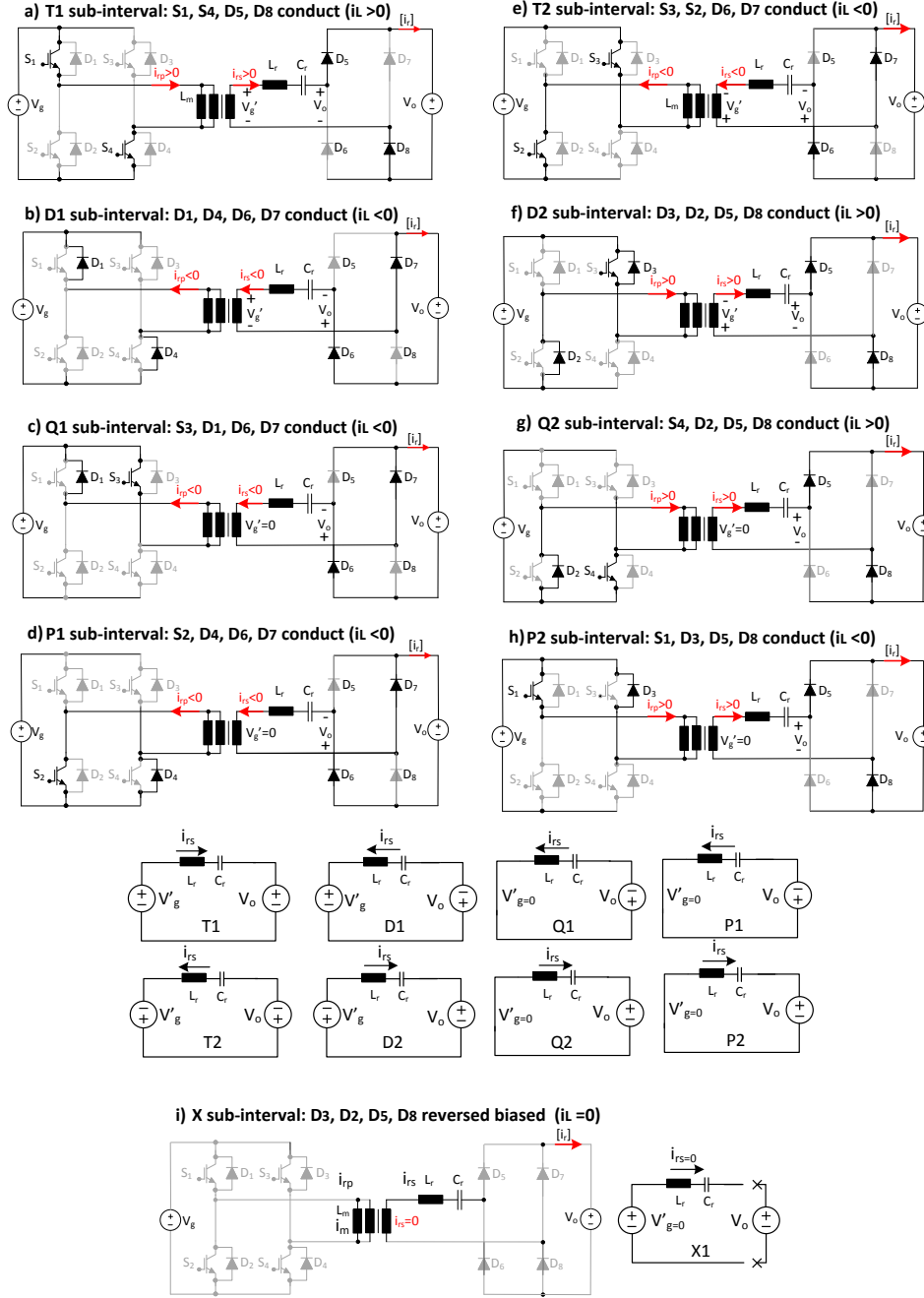


Fig. 11. Equivalent circuits for SRC# subintervals : T1 (a); D1 (b); Q1 (c); P1 (d); T2 (e); D2 (f); Q2 (g); P2 (h); X (i).

$F_{sw} \geq F_r/2$, transition to CCM1 mode will occur.

A one-cycle operation of SRC# is (regardless of conduction mode) composed of a sequence of linear circuits, each corresponding to a particular switching interval, as seen in Table IV. Every linear circuit is determined by switching certain switch pairs, as described in Fig. 11(a to i) and in Table V. For even further clarification, Fig. 12 (a, b, c, d) presents secondary and primary resonant currents with their corresponding conductive devices per sub-intervals for every mode of operation.

TABLE III
SRC# CONDUCTION MODES AND BOUNDARY CONDITIONS

Mode of operation	Range of switching frequency	V_{Cr}
DCM1	$0-F_r$	$< V_o$
DCM2	$0-F_r/2$	$> V_o$
CCM1-hybrid	$F_r/2 - F_r$	$< V_g' + V_o$
CCM1	$F_r/2 - F_r$	$> V_g' + V_o$

A. Equations for subintervals

The time domain approach is used to investigate the behaviour of the SRC# operated with variable frequency and

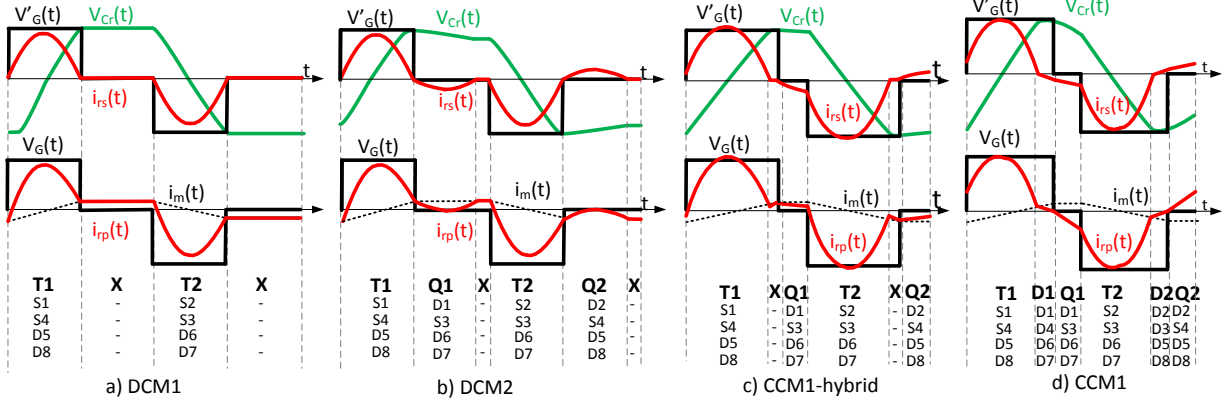


Fig. 12. Secondary (top) and primary (bottom) resonant currents with their respective conductive devices per sub-intervals in DCM1 (a); in DCM2 (b); in CCM1-hybrid (c) and in CCM1 (d).

TABLE IV
SEQUENCE OF SUBINTERVALS FOR DIFFERENT MODES

Mode of operation	Subinterval sequence
DCM1	T1-X-T2-X
DCM2	T1-Q1-X-T2-Q2-X
CCM1-Hybrid	T1-X-Q1-T2-X-Q2
CCM1	T1-D1-Q1-T2-D2-Q2

TABLE V
CONDUCTING DEVICES FOR DIFFERENT SUB-INTERVALS

Subinterval	T1	D1	Q1	P1	T2	D2	Q2	P2	X
Inverter	S1	D1	D1	S2	S2	D2	D2	S1	-
Side	S4	D4	S3	D4	S3	D3	S4	D3	-
Rectifier	D5	D6	D6	D6	D6	D5	D5	D5	-
Side	D8	D7	D7	D7	D7	D8	D8	D8	-
V'_g sign	+	+	0	0	-	-	0	0	0
V_o sign	+	-	-	-	-	+	+	+	0
V_t sign	+	+	+	+	-	-	-	-	0

phase shift modulation. From the equivalent circuits, steady state equations of resonant inductor and capacitor voltage for every mode are derived by Laplace transform. Considering the half wave symmetry of tank variables, the analysis is performed for half cycle of switching period for every mode of operation. Similar to [20] the circuit behaviour of the SRC# under each topological mode can be described using the following differential equations, for subintervals T1, D1, T2, D2, Q1, Q2, P1, P2 and X, where V_t is the resonant tank

voltage:

$$L_r \frac{di_{rs}}{dt} + V_{Cr} = V_t \quad (8)$$

$$C_r \frac{dV_{Cr}}{dt} = i_{rs} \quad (9)$$

$$V_t = \begin{cases} V'_g - V_o, & \text{for } T1 \\ V'_g + V_o, & \text{for } D1 \\ +V_o, & \text{for } Q1 \\ -V'_g + V_o, & \text{for } T2 \\ -V'_g - V_o, & \text{for } D2 \\ -V_o, & \text{for } Q2 \\ V_{Co}, & \text{for } X \end{cases} \quad (10)$$

For subinterval X:

$$L_r \frac{di_{rs}}{dt} = 0 \quad (12)$$

$$C_r \frac{dV_{Cr}}{dt} = 0 \quad (13)$$

By solving equations eq. (8) and eq. (9), expressions for i_{rs} and V_{Cr} in each subinterval can be derived, with application of the consistent initial conditions for each subinterval:

$$i_{rs} = \frac{V_t - V_{Cr}(t_0)}{Z_c} \sin \omega_r t + i_{rs}(t_0) \cos \omega_r t \quad (14)$$

$$V_{Cr} = V_t - (V_t - V_{Cr}(t_0)) \cos \omega_r t + i_{rs}(t_0) Z_c \sin \omega_r t \quad (15)$$

Considering that $V_t = V'_g - V_o$, the polarity of V_t is determined by the specific sub-intervals and conductive devices, as seen in Table. V.

B. DCM1

With reference to Fig. 14, DCM1 mode can appear in the full switching range and it's possible only if $\Delta V \approx 0$ and $V_{Cr} \leq V'_g$. Fig. 14 shows on top the inverter voltage reflected on rectifier side V'_g , rectifier voltage V_o and secondary resonant current i_{rs} . Middle graph describes resonant capacitor voltage

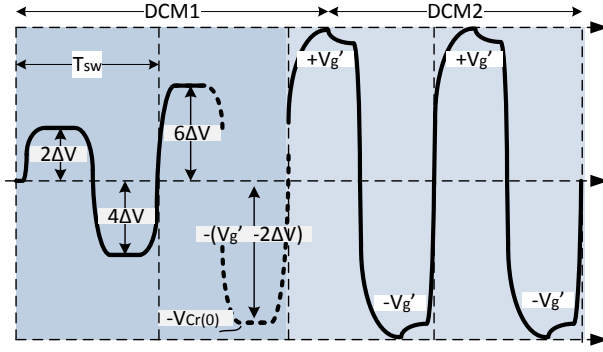


Fig. 13. Transition of capacitor voltage V_{Cr} from DCM1 to DCM2.

V_{Cr} , while lower graph indicates the transistors (S1 to S4) switching pattern.

This mode of operation is composed of following sub-intervals: T1-X-T2-X. The sub-intervals equivalent circuits are shown in Fig. 11 (a), (e) and (i). Due to symmetry of operation over an entire switching interval, the analysis is performed out over half the switching interval.

1) *Sub-interval T1*: $t_0 \leq t \leq t_1$ This sub-interval starts when both S1 and S4 conduct, exciting the resonant tank with positive voltage V_g' . On the rectifier side, D5 and D8 are forward biased and the tank will be exposed to the rectifier voltage V_o . A positive inductor current rises from 0 with di/dt limited by the resonant tank elements, as long as $V_g' > V_o$. At $t_0 = 0$, the inductor current is zero due to the discontinuous nature of the inductor current in this mode. Resonant capacitor voltage rises from a negative V_{Cr} towards a positive value. So, both i_{rs} and V_{Cr} increase to positive values. This ensures ZVS turn-on on inverter side switches S1 and S4 and for rectifier side diodes. During this sub-interval a half resonant cycle (of duration $T_r/2$) is allowed to pass. T1 sub-interval finishes when S4 is blocked and S3 starts conducting. By this time, the resonant current has reached zero while capacitor voltage stabilizes at $+V_g'$ (considering the initial condition for $V_{Cr}(t_0) = -V_g' + 2\Delta V$ and $t = \pi$, see Fig. 13). Following equations are expressions for resonant current and voltage in DCM1 T1 sub-interval:

$$i_{rs}(t) = \frac{V_g' - V_o - V_{Cr}(t_0)}{Z_c} \sin \omega_r t \quad (16)$$

$$V_{Cr}(t) = (V_g' - V_o) - (V_g' - V_o - V_{Cr}(t_0)) \cos \omega_r t \quad (17)$$

As seen in Fig. 13, during transient state, capacitor voltage is increasing every switching interval with $2 \cdot \Delta V$ from 0 to $+V_g'$. As soon as $V_{Cr} \geq V_g'$, transition to DCM2 occurs.

2) *Sub-interval X*: $t_1 \leq t \leq t_2$ X sub-interval begins when S1 and S3 both conduct, while S2 and S4 are blocked. This means V_g' is clamped to zero, inductor current remains at zero and all rectifier diodes are reversed biased. The equivalent circuit of this sub-interval can be seen as an open circuit resonant tank. In this time, V_o drops to V_{Cr} level. One half cycle is finished as soon as S1 is blocked, while S2 and S3

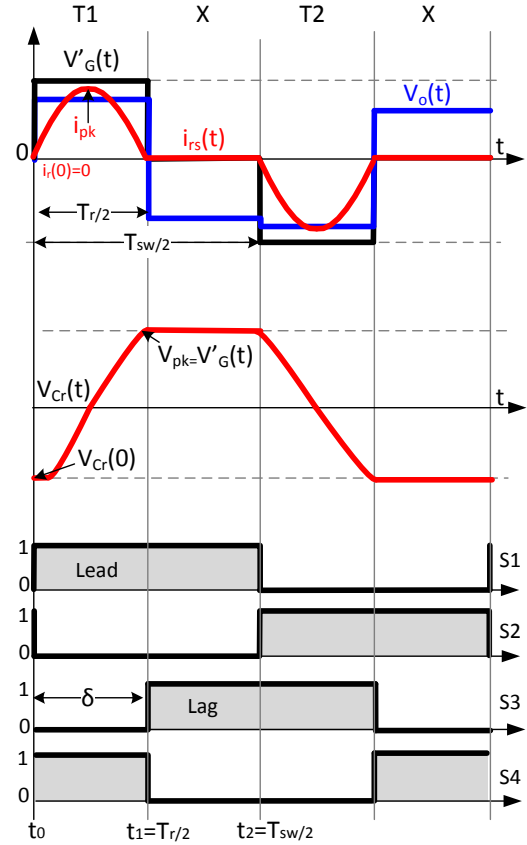


Fig. 14. DCM1 characteristic waveforms: top - inverter voltage reflected on rectifier side V_g' , rectifier voltage V_o , resonant secondary current i_{rs} ; middle - resonant capacitor voltage V_{Cr} ; bottom - corresponding switching pattern.

conduct. Following sub-intervals T2 and X are analysed with similar procedure.

$$i_{rs}(t) = 0 \quad (18)$$

$$V_{Cr}(t) = V_g' \quad (19)$$

3) *Power flow*: To evaluate how much power is delivered during DCM1, the average area of current waveforms i_{rs} during T1 and X sub-interval has to be calculated, following the steps from eq. (20) to eq. (26):

$$i_{out} = \langle i_{rs}(t) \rangle_{T_{sw}} = \frac{2}{T_{sw}} \int_{t_0}^{t_2} i_{rs}(t) dt \quad (20)$$

$$i_{out} = 2 \cdot F_{sw} \cdot q_s \quad (21)$$

$$q_s = 2 \cdot C_r \cdot V_{Cr} \quad (22)$$

$$i_{out} = 4 \cdot F_{sw} \cdot C_r \cdot V_{Cr} \quad (23)$$

$$P_{out} = V_{out} \cdot i_{out} \quad (24)$$

$$V_{Cr} = V_g' = V_{in} \cdot N \quad (25)$$

$$P_{out} = 4 \cdot F_{sw} \cdot N \cdot C_r \cdot V_{in} \cdot V_{out} \quad (26)$$

Comparing eq. (26) to eq. (6), they differ by a factor of 2. The main reason is that capacitor voltage on the "classic" SRC (with LC tank on inverter side) stabilizes at $2 \cdot V_g'$. For

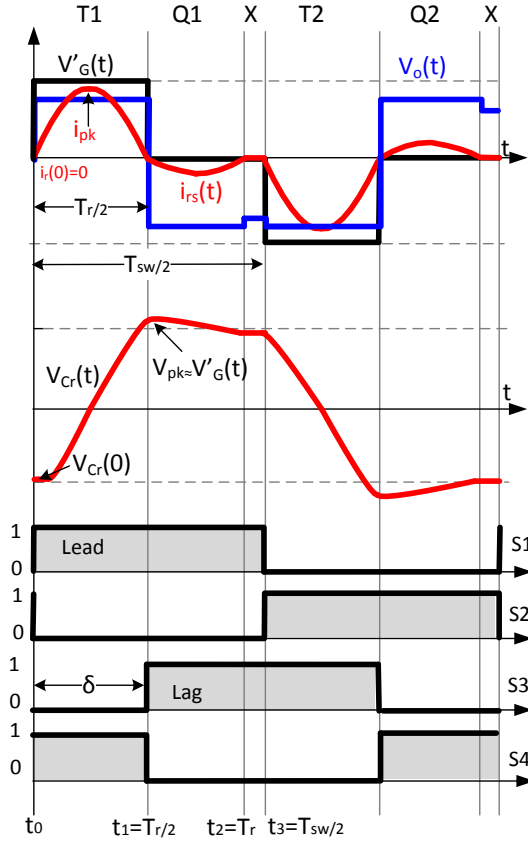


Fig. 15. DCM2 characteristic waveforms: top - inverter voltage reflected on rectifier side V_g' , rectifier voltage V_o , resonant secondary current i_{rs} ; middle - resonant capacitor voltage V_{Cr} ; bottom - corresponding switching pattern.

the classic SRC, there are no Q1 or Q2 sub-intervals (no pulse removal), but only D1 or D2 sub-intervals. The transition from T1 to D1 will occur, only if $V_{Cr} \geq (V_g + V_o')$.

C. DCM2

With respect to Fig. 15, principle waveforms for DCM2 are shown. As the name implies two half resonant cycles will appear during a half switching period. This conduction mode can only appear in the interval $[0, T_r/2]$ and if $\Delta V > 0$. Being very similar to DCM1, DCM2 is a sequence of following sub-intervals: T1-Q1-X-T2-Q2-X, with Q1 and Q2 equivalent sub-circuits shown in Fig. 11(c) and (g). Due to half cycle symmetry only the first three sub-intervals will be analysed, as the other three are similar but with opposite voltage and current signs.

1) *Sub-interval T1*: $t_0 \leq t \leq t_1$ As S4 is already conducting, S1 switch is turned on and a full resonant cycle is delivered to the load, while D5 and D8 are forward biased. During this interval, as the resonant current i_{rs} is increasing from 0, resonant capacitor voltage increases too from $-V_{Cr}$. At $t_1 = T_r/2$, T1 sub-interval is finished, having again a zero inductor current and maximum V_{Cr} . Resonant inductor current and capacitor voltage equations are similar to DCM1 mode.

2) *Sub-interval Q1*: $t_1 \leq t \leq t_2$ During Q1 sub-interval, the inductor current resonates for another half cycle, until $t_2 = T_r$. During this period, S1 is still on, but S4 is blocked and S3 starts to conduct. Therefore, the negative current flows through D1 and T3 as seen in Fig. 11(c). On rectifier side, D6 and D7 are forward biased and due to this rectifier voltage V_o is negative. Capacitor voltage is slowly discharged, as $V_{Cr} > V_o$. Resonant current and capacitor voltage are given in Eq. (27) and (28). Eq. (29) shows where capacitor voltage will stabilize, when $t = t_2 = T_r$.

$$i_{rs}(t) = \frac{V_o - V_{Cr}(t_1)}{Z_c} \sin \omega_r(t - t_1) \quad (27)$$

$$V_{Cr}(t) = V_o - (V_o - V_{Cr}(t_1)) \cos \omega_r(t - t_1) \quad (28)$$

$$V_{Cr}(t) = V_o - (V_o - V_g')(+1) = V_o - \Delta V \quad (29)$$

3) *Sub-interval X*: $t_2 \leq t \leq t_3$ When $V_{Cr} = V_o - \Delta V$, another X subinterval begins as resonant current is zero, while all rectifier diodes are reversed biased. At $t_3 = T_{sw}/2$, switch S1 is off and another half cycle begins. Similar to DCM1, in this sub-interval, the resonant current is zero and capacitor voltage stays flat, meaning no power is delivered to V_{out} .

4) *Power flow and peak stress*: Equation for power flow is exactly the same as in DCM1. As in DCM1 and also according to [14], the SRC# is operating similar to a frequency controlled current source in DCM2, implying a linear function between power and frequency. On the other hand, the slope of the function is slower as compared to DCM1, due to higher ΔV across the LC tank. In DCM2, V_{out} is smaller than in DCM1. This means output power will also be less, but still proportional to the frequency. Looking at Fig. 19a, one notices the slope in DCM2 is proportional to ΔV and also impacts the resonant peak current (Fig. 19b).

5) *Boundary condition*: Transition from DCM1 to DCM2 is achieved when:

$$V_{Cr} > V_o \quad (30)$$

D. CCM1-Hybrid

CCM1-hybrid mode of conduction is described in Fig. 16. The name *hybrid* is used as very short X sub interval (characterized by zero resonant current) will appear. First of all, this mode can appear in the switching interval $[T_r/2, T_r]$ and if $\Delta V \approx 0$. It is composed of following subintervals: T1-X-Q1-T2-X-Q2. Similar to other modes of operation, only the first three sub-intervals will be analysed, as the other three are similar but with opposite voltage and current signs.

1) *Sub-interval T1*: $t_0 \leq t \leq t_1$

During subinterval T1, resonant current i_{rs} will start at a low turn on current $i_r(t_0)$ and for a period equal to $\delta \cdot T_{sw}/2$ a resonant cycle is delivered to the load, as switches S1 and S4 conduct both. Capacitor voltage increases from a negative V_{C0} towards a positive value. Resonant current and capacitor voltage are determined as:

$$i_{rs} = \frac{V_g' - V_o - V_{Cr}(t_0)}{Z_c} \sin \omega_r t + i_{rs}(t_0) \cos \omega_r t \quad (31)$$

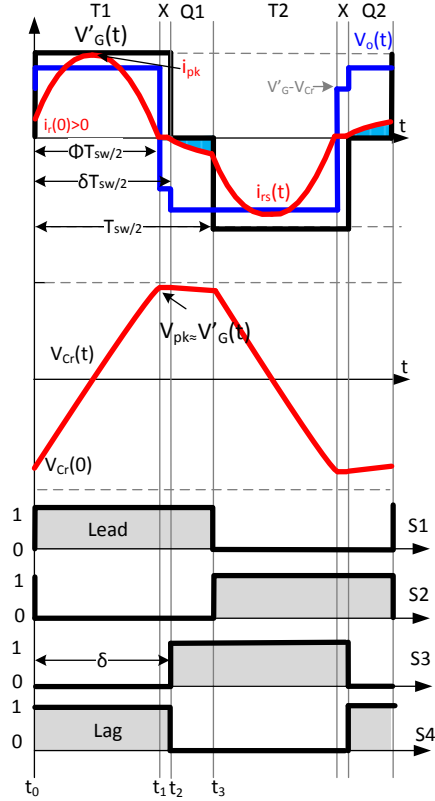


Fig. 16. CCM1-Hybrid characteristic waveforms: top - inverter voltage reflected on inverter side V'_g , rectifier voltage V_o , resonant secondary current i_{rs} ; middle - resonant capacitor voltage V_{Cr} ; bottom - corresponding switching pattern.

$$V_{Cr} = (V'_g - V_o) - (V'_g - V_o - V_{Cr}(t_0)) \cos \omega_r t + i_{rs}(t_0) Z_c \sin \omega_r t \quad (32)$$

The sub-interval ends at t_1 , as for a very short period, V_{Cr} is equal to rectifier voltage V_o and no current is delivered to the load.

2) *Sub-interval X*: $t_1 \leq t \leq t_2$

Next, a different kind of X subinterval appears, as V'_g is still applied. The reason for it is that $V_{Cr} \leq (V'_g + V_o)$. The length of T1 and X subintervals equals with $\delta \cdot T_{sw}/2$ which is the phase displacement between the inverter legs. The sub-interval ends at t_2 , when switch S4 is blocked and switch S3 starts conducting.

$$i_{rs} = 0 \quad (33)$$

$$V_{Cr} = V_t \quad (34)$$

$$V_{out} = V'_g - V_{Cr} \quad (35)$$

3) *Sub-interval Q1*: $t_2 \leq t \leq t_3$

Further on, as soon as phase displacement is implemented, a Q1 subinterval will begin and negative resonant current will start to flow. Here, V'_g is clamped to zero and tank voltage V_t equals V_o . From switching point of view, the inverter switches and rectifier diodes turn on at a low current and turn-off

with ZCS. Resonant tank current and voltage are described in following equations.

$$i_{rs} = \frac{V_o - V_{Cr}(t_2)}{Z_c} \sin \omega_r(t - t_2) + i_{rs}(t_2) \cos \omega_r(t - t_2) \quad (36)$$

$$V_{Cr} = V_o - (V_o - V_{Cr}(t_2)) \cos \omega_r(t - t_2) + i_{rs}(t_2) Z_c \sin \omega_r(t - t_2) \quad (37)$$

Following T2, X and Q2 subintervals are complementary, but with opposite sign.

4) *Power flow*: Compared to DCM1, the power to frequency relation in CCM1-hybrid is slightly non linear and described in Eq. 42.

$$M = \frac{V_o/N}{V_g} \quad (38)$$

$$\gamma = \frac{F_r \cdot \pi}{F_{sw}} \quad (39)$$

$$\Phi = 1 + \frac{2 \cdot \text{atan}\left(\frac{(V_g + \cos(\gamma) \cdot (2 \cdot V_o - V_g))}{(\sin(\gamma) \cdot (2 \cdot V_o - V_g))}\right)}{\gamma} \quad (40)$$

$$A = \frac{(1 - \cos(\Phi\gamma)) \cdot ((2M - 1) \cdot \cos(\gamma) + 1)}{\cos(\gamma) - \cos(\Phi\gamma)} \quad (41)$$

$$P_{out} = V_g^2 \cdot \omega_{sw} \cdot C_r \cdot \frac{1}{\pi} \cdot A \quad (42)$$

5) *Boundary condition*: Transition from CCM1-hybrid to CCM1 is achieved when:

$$V_{Cr} > V'_g + V_o \quad (43)$$

E. CCM1

Final mode of conduction is characterized by the waveforms from Fig. 17 and it's composed of following subintervals: T1-D1-Q1-T2-D2-Q2, with D1 and D2 equivalent circuits shown in Fig. 11(b) and (f). This mode appears only above $F_r/2$ and if $\Delta V \gg 0$, showing a highly nonlinear relation between power and switching frequency and it should be avoided as it increases turn-on losses. Only first half cycle is analysed as the other half cycle is symmetric and complementary.

1) *Sub-interval T1*: $t_0 \leq t \leq t_1$ Similar to CCM1-hybrid, T1 sub-interval starts at a current $i_{rs} > 0$, but with larger magnitude, impacting turn-on losses. Also in this sub-interval a resonant cycle is delivered to the load until $t = t_1$, when the resonant current reaches zero and capacitor voltage is reaching it's peak value. Lower equations describes the two parameters.

$$i_{rs} = \frac{V'_g - V_o - V_{Cr}(t_0)}{Z_c} \sin \omega_r t + i_{rs}(t_0) \cos \omega_r t \quad (44)$$

$$V_{Cr} = (V'_g - V_o) - (V'_g - V_o - V_{Cr}(t_0)) \cos \omega_r t + i_{rs}(t_0) Z_c \sin \omega_r t \quad (45)$$

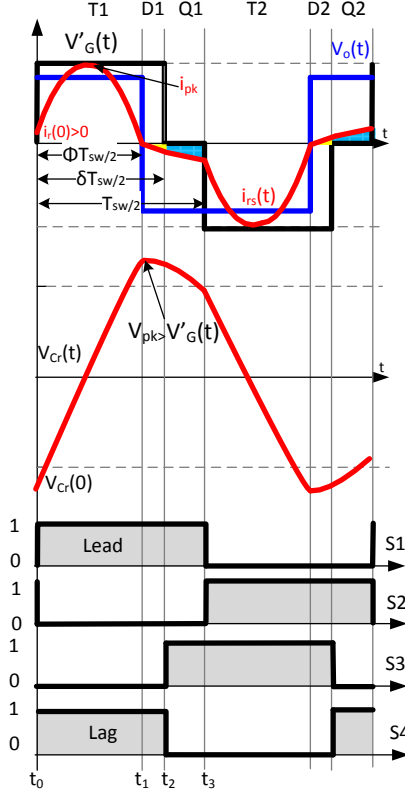


Fig. 17. CCM1 characteristic waveforms: top - inverter voltage reflected on inverter side V'_g , rectifier voltage V_o , resonant secondary current i_{rs} ; middle - resonant capacitor voltage V_{Cr} ; bottom - corresponding switching pattern.

2) Sub-interval D1: $t_1 \leq t \leq t_2$

As a positive V'_g is still applied to transformer windings and $V_{Cr} > V_0$, a negative current flows through the resonant tank. This means on inverter side, diodes D1, D4 are conducting, while on rectifier side D6 and D7 are forward biased. The capacitor voltage is slowly discharging. Equations for resonant current and capacitor voltage are described as follows:

$$i_{rs} = \frac{V'_g + V_o - V_{Cr}(t_1)}{Z_c} \sin \omega_r(t - t_1) + i_{rs}(t_1) \cos \omega_r(t - t_1) \quad (46)$$

$$V_{Cr} = (V'_g + V_o) - (V'_g + V_o - V_{Cr}(t_1)) \cos \omega_r t + i_{rs}(t_1) Z_c \sin \omega_r(t - t_1) \quad (47)$$

Sub-interval D1 is ended at $t = t_2$, when switch S4 is turned off and S3 is turned on.

3) Sub-interval Q1: $t_2 \leq t \leq t_3$ By turning off switch S4, applied inverter voltage V_g is clamped to zero. A negative current is still flowing, but through switch S3 and diode D1, while D6 and D7 are still forward biased. The capacitor voltage is still discharging. This sub-interval will end at $t = t_3$,

when switch S1 is turned-off and S2 is turned-on. Equations for resonant current and capacitor voltage are given below:

$$i_{rs} = \frac{V_o - V_{Cr}(t_2)}{Z_c} \sin \omega_r(t - t_2) + i_{rs}(t_2) \cos \omega_r(t - t_2) \quad (48)$$

$$V_{Cr} = V_o - (V_o - V_{Cr}(t_2)) \cos \omega_r(t - t_2) + i_{rs}(t_2) Z_c \sin \omega_r(t - t_2) \quad (49)$$

4) Power flow: Considering the power flow equation for CCM1 mode of operation, eg. (50) is derived. In CCM1, the relation between power and frequency is highly non-linear, making this mode of operation not favourable.

$$P_{out} = V_g^2 \cdot \omega_{sw} \cdot C_r \cdot M \cdot \frac{2}{\pi} \cdot B \quad (50)$$

$$B = \left[\frac{\cos(\gamma) - 1 + 2M \cos(\gamma(1 - \Phi))}{-\cos(\gamma(1 - \Phi)) - \cos(\gamma)} \right] \cdot \cos(\Phi\gamma) + M \cdot (\cos \Phi\gamma + 1) \quad (51)$$

$$\Phi = \frac{\delta}{2} + \frac{1}{\lambda} \cdot Q_s \cdot \sin M \quad (52)$$

F. Resonant tank stress

For proper component selection, the peak stress level has to be considered. The peak current level will occur in sub-interval T1 at $\pi/2$, while peak voltage at π . Considering Eq. (53) to (57), following parameters are defined: normalized output voltage M , converter quality factor Q_s , normalized switching frequency γ , constant K and load resistance R_{load} . The equations are valid for all modes of operation.

$$M = \frac{V_o/N}{V_g} \quad (53)$$

$$K = \frac{Q_s \cdot \gamma}{2} \quad (54)$$

$$Q_s = \frac{1}{\omega_r \cdot C_r \cdot R_{load}} \quad (55)$$

$$\gamma = \frac{F_r \cdot \pi}{F_{sw}} \quad (56)$$

$$R_{load} = \frac{V_{out}^2}{P_{out}} \quad (57)$$

Similar to [14] eq. (58) and (59) will predict the peak resonant tank voltage V_{pk} and current stress I_{pk} in all modes of operation.

$$I_{pk} = \omega_r \cdot C_r \cdot V_g \cdot (M(K + 1) - 1) \quad (58)$$

$$V_{pk} = M \cdot K \cdot V_g \cdot N \quad (59)$$

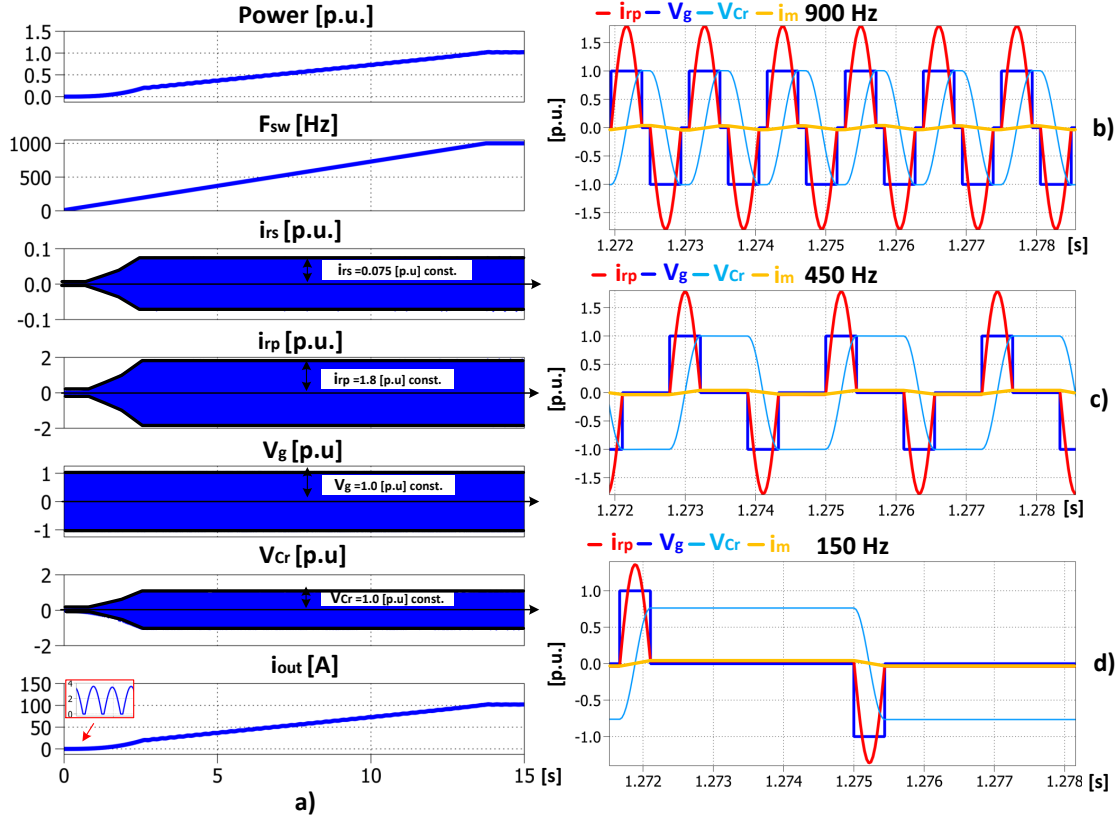


Fig. 18. Simulation results: steady state operation in DCM1 with steps in switching frequency (a); zoomed in windows of principle waveforms (primary resonant current i_{rp} , magnetizing current i_m , inverter voltage V_g and resonant capacitor voltage V_{Cr} at 900 Hz (b), 450 Hz (c) and 150 Hz (d).

V. STEADY STATE OPERATION

To illustrate the steady state operation of the target converter, a PLECS simulation model was built and runned at different switching frequencies, in the range 0 to 1000 Hz, while voltage difference ΔV between input and output voltage was close to 0.1%, facilitating the operation in DCM1. The results are shown in Fig. 18 and point out that output power is related to the applied switching frequency (cf. Fig. 18 a, b). As the converter operates in DCM1, peak resonant current and voltage are constant in the whole operating range. Fig. 18 b, c and d are zoomed in windows of the principle current and voltage waveforms (primary current i_{rp} , secondary current i_{rs} , inverter voltage V_g , capacitor voltage V_{Cr} , magnetizing current i_m) and they also demonstrate how pulse removal technique impacts the magnetizing current, keeping it constant, regardless of applied frequency. Another aspect worthy to mention is that at very low switching frequency $F_{sw} < 50$ Hz, the converter output current becomes discontinuous, as seen in Fig. 18a-(bottom).

VI. PEAK RESONANT CURRENT AND VOLTAGE STRESS

Peak current and voltage will determine the specifications for semiconductors and resonant tank parameters. Evaluation of stress is determined through the analytical equations from previous section and through steady state and dynamic simulations. Fig. 19(a,b and c) shows the good agreement between

analytical values and simulation results, within operation range of 0 to 1000 Hz and for different ΔV values. Looking at Fig. 19a, a power to frequency characteristic in DCM1 is shown on the black line, with a linear characteristic. As soon as a ΔV is increased, the characteristic starts to be non-linear at the end point. In Fig. 19(b and c), if operation in DCM1 is considered, the peak current and voltage are the same in full switching interval. Applying a ΔV , will impact both current and voltage peak. It is observed in Fig. 19e, how ΔV is impacting current waveform and it's peak, while the converter operates at the same frequency of 900 Hz. For this case, the converter can operate close to DCM1, while having a ΔV of 5%. Further on, Fig. 19f concludes the fact that capacitor voltage is output power dependent. Assuming a max. ΔV of 10%, with relation to Fig. 19a, nominal power is now being delivered at ≈ 825 Hz. At the same frequency, it is noticed that peak current has increased from 1.8 p.u. to 2.1 p.u., while capacitor voltage from 1.0 p.u. to 1.25 p.u. . This means, when designing the converter LC tank, one has to consider a variation of +25% above nominal voltage and current specifications, to allow a safe margin with a 10% output voltage variation. Another aspect necessary to mention is that the converter efficiency will decrease for a ΔV higher then 5%.

Fig. 20 (a, b, c, d) indicates the trajectories of resonant capacitor voltage V_{Cr} in relation to resonant secondary current i_{rs} for every mode of operation.

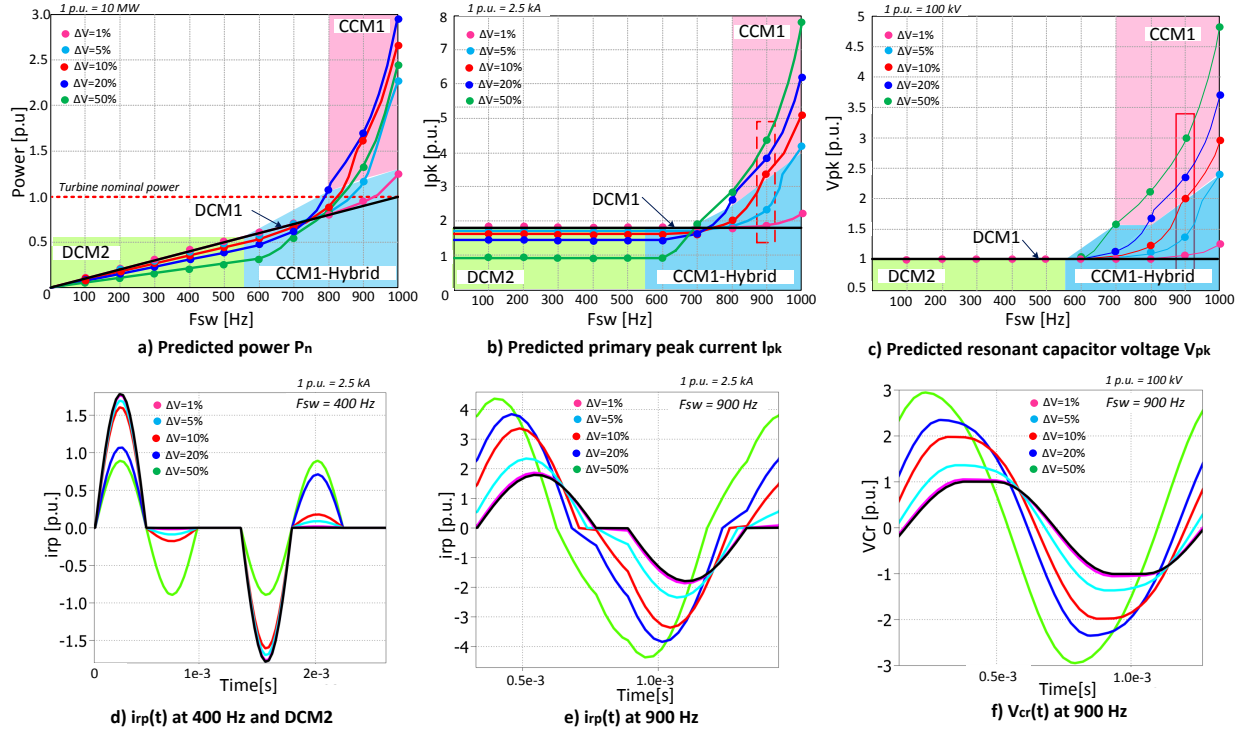


Fig. 19. Impact of ΔV (voltage difference between V_g' and V_o) on: output power P_n (a); primary resonant current peak I_{pk} (b); resonant capacitor voltage peak V_{pk} (c); primary resonant current i_{rp} in DCM2 (e); primary resonant current i_{rp} at 900 Hz (f); resonant capacitor voltage waveform V_{cr} (g).

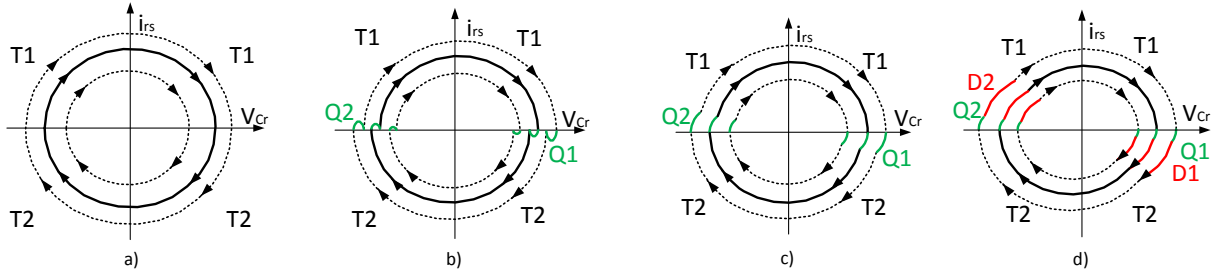


Fig. 20. Trajectory of resonant capacitor voltage V_{Cr} in relation to resonant secondary current i_{rs} in : DCM1 (a); DCM2 (b); CCM1-hybrid (c) and CCM1 (d).

VII. EXPERIMENT AND DISCUSSIONS

A. Experimental setup

The SRC# has been built and tested at relatively low power ratings (see Table VI), to confirm modes of operation, control principles and basic protection based on voltage and current monitors. Loss model validation will be performed on a higher power and voltage demonstrator and presented in future publication.

The circuit diagram is shown in Fig. 21a and experimental setup in Fig. 21b. The transformer (1:2 turns ratio) is designed for a maximum frequency of 1000 Hz, which is the same as the target component, and uses an amorphous core and windings with round wires. The low scale setup was tested with two different ΔV and variable switching frequencies. The measuring equipment was a Lecroy HDO4054 oscilloscope,

with high voltage differential probes (ADP305) and current probes. Fig. 22 show the SRC# characteristic waveforms for DCM1 mode, where $\Delta V \approx 0$.

Looking at principle waveforms from Fig. 22 (right column), it can be noticed that regardless of switching frequency, the magnetizing current is stable and there is no saturation phenomenon. As the transformer windings resistance is high in this case, as compared to the magnetizing inductance L_m , the magnetizing current shows a slow decline during the zero voltage period. i_m was recorded, while the transformer secondary was in open circuit and afterwards overlapped across the i_{rp} measured data.

Fig. 22 shows the secondary resonant current (left column) and primary resonant current (right column) (i_{rp} and i_{rs}) and applied inverter voltage V_g for three different switching frequencies (200, 500 and 800 Hz). It is noticed in fig. 22 (right

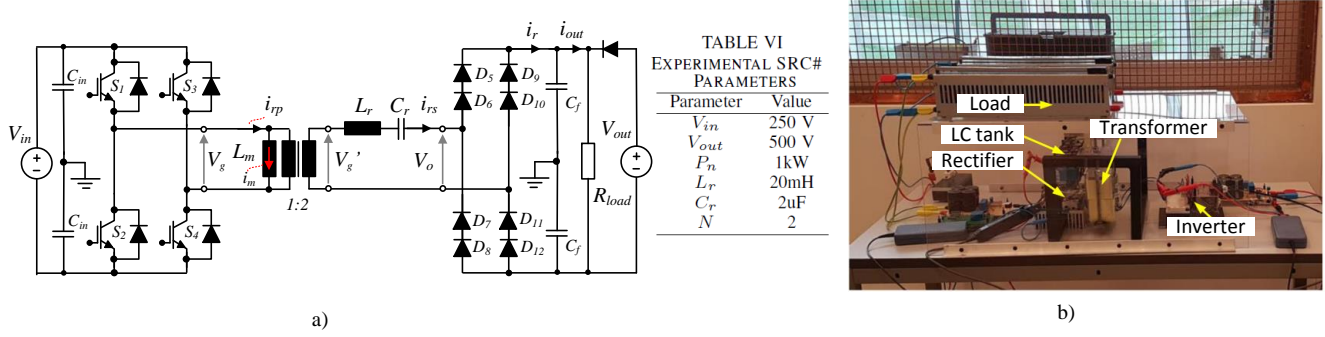


Fig. 21. Experiment circuit diagram (a) and laboratory setup (b). In order to have a constant output voltage, a second DC source is used to supply a load resistor. As long as V_g' is smaller than V_o no power is delivered to load, as it comes only from V_o . If for example, the SRC# will deliver 50% of nominal load, then the external dc source will cover the rest of 50%. In this manner it's possible to obtain a constant output voltage without too much effort. The disadvantage is that the resistors are always dissipating nominal power.

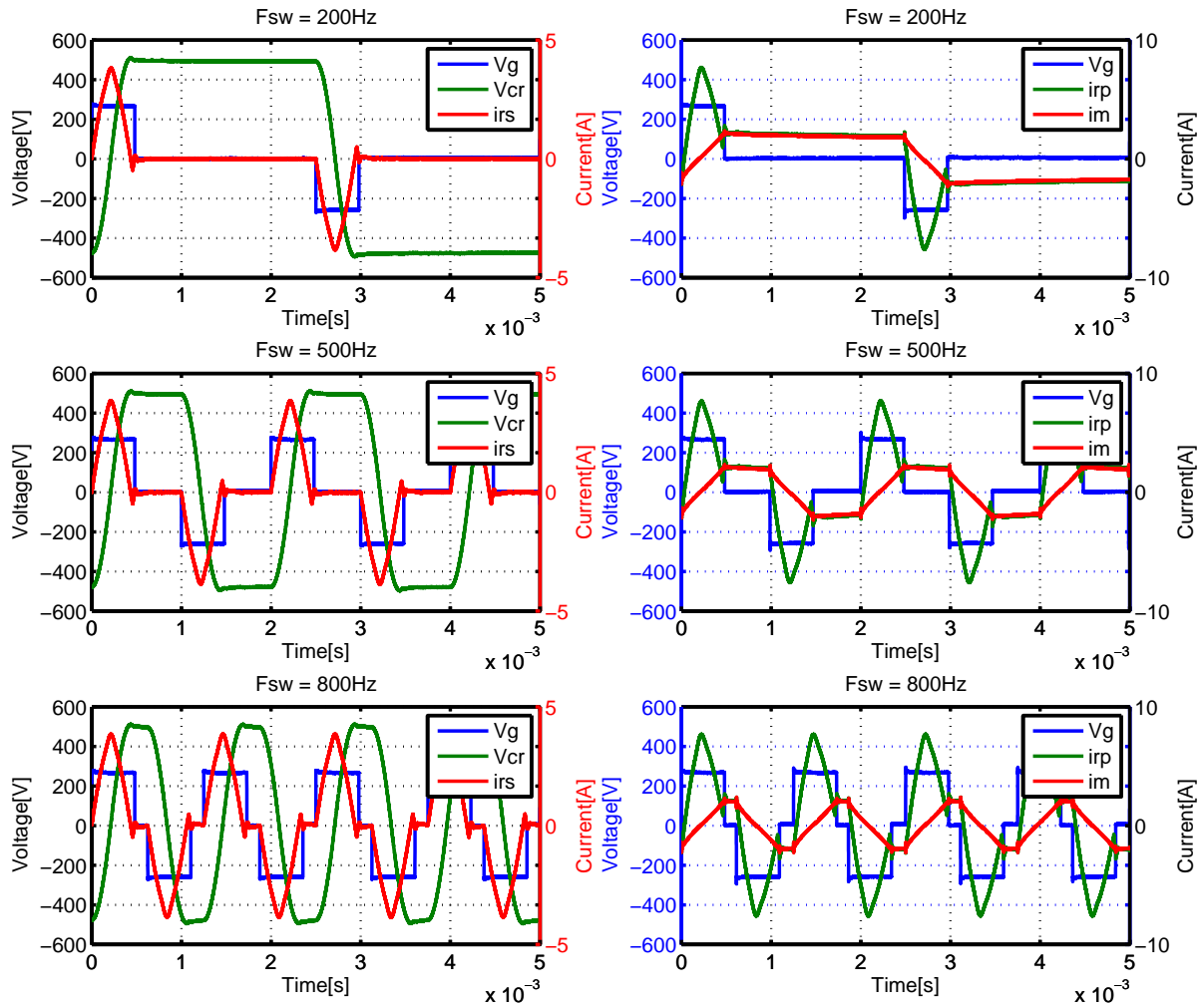


Fig. 22. Experimental results with $\Delta V \approx 0$. (Left column) Measured secondary side resonant current i_{rs} , resonant capacitor voltage V_{cr} and inverter voltage V_g . (Right column) measured primary side resonant current i_{rp} , magnetizing current i_m and inverter voltage V_g for different switching frequencies.

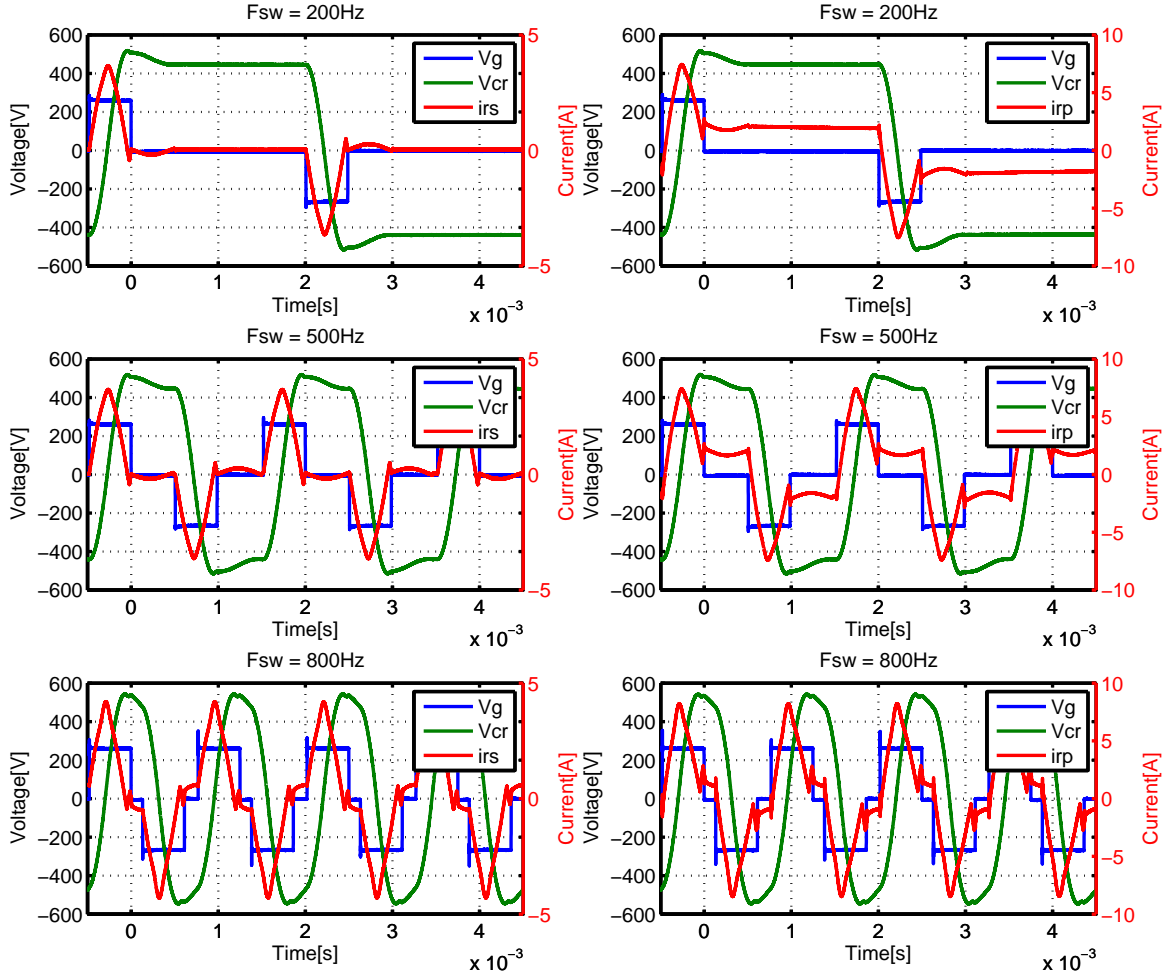


Fig. 23. Experimental results with $\Delta V \approx 10\%$. (Left column) Measured secondary side resonant current i_{rs} , resonant capacitor voltage V_{Cr} and inverter voltage V_g . (Right column) Measured primary side resonant current i_{rp} , magnetizing current i_m and inverter voltage V_g (right side) for different switching frequencies.

column), that during the zero voltage periods, on inverter side the current flowing through one pair of transistor and diodes (D1, S3 for positive current and D2, S4 for negative current) is the magnetizing current. Now, observing the secondary resonant current at turn-off in Fig. 22 (left column), the impact of diodes reverse recovery is shown. As mentioned earlier in the design process, a certain holding time T_{rec} needs to be taken in consideration to allow reverse recovery process. Another phenomenon observed during the experiments, is the acoustic noise generates, as the converter operates from very low frequency up to 1000 Hz. For elevated power, it is expected the noise to increase and it will require a system to damp the noise.

Fig. 23 presents the same waveforms (V_g , V_{Cr} , i_{rp} and i_{rs}) as in Fig. 22, but for a $\Delta V \approx 10\%$. The top and middle graphs show operation in DCM2, while bottom graphs in CCM1-hybrid. As the voltage drop between V_g' and V_o is 10%, there is no longer a linear relation between switching frequency F_{sw} and output power P_{out} . E.g, the peak in i_{rs} at 800 Hz is $\approx 4A$,

while at 200 Hz it is 3.3A, meaning a difference of $\approx 20\%$.

B. Discussions

Beside the benefits from controlling LV DC bus link, from soft-switching commutation, from compact transformer size and from a high voltage rectifier assembled with line frequency diodes, the SRC# circuit also presents its drawbacks: only single circuit configuration seems possible, precluding the use of a three-phase, three-limb transformer. Moving the resonant tank to the rectifier side, the transformer risks saturation. This is due to imbalanced (dc offset) from the inverter, caused by the secondary effects like differences in inverter phase-leg voltage drops and commutation time characteristics. Options to mitigate this dc offset include asymmetric duty cycle control or on-line monitoring of the magnetizing flux with a "magnetic ear", as proposed in [34].

VIII. CONCLUSION

The series resonant converter with resonant tank on high voltage side is proposed as a candidate for megawatt high-voltage DC wind turbines, due to high efficiency and low transformer size. In order to control output power and increase efficiency, frequency control in sub resonant is identified as an optimal control method for high power resonant topologies. But the drawback is that the transformer needs to be designed for lowest operating point. In order to solve this issue, a new method of operation, entitled pulse removal is introduced. Variable frequency and phase shift in sub resonant mode are used to control output power and the main principle is to clamp the applied voltage to zero as soon as the resonant current becomes zero, limiting the flux build-up on transformer core. The paper has focused on the analyse of SRC# and discusses the conduction modes the topology might experience, for different output voltage drops. For every mode, resonant current and voltage equations were presented, together with predictions of output power, peak voltage and current stress. Pulse removal technique and the expected conduction modes were examined on a 1kW, 500V prototype. Loss segregation and closed-loop control will be investigated experimentally and presented in future publication, on a higher power and voltage ratings demonstrator.

REFERENCES

- [1] C. Meyer, *Key Components for Future Offshore DC Grids*. Ph.D. dissertation, Inst.Pow.Electr.Driv., RWTH Aachen University, 2007.
- [2] C. Meyer and Rik W. De Doncker, *Design of three phase series resonant converter for offshore DC Grids*. IEEE Ind. Appl. Ann. Meet., 2007., pp.216-223.
- [3] L. Max, *Design and Control of A DC Grid for Offshore Wind Farms*. Ph.D. dissertation, Dept. Energ. Env., Chalmers University of Tech., 2009.
- [4] W.Chen, A.Q.Huan, C.Li, G.Wang and W.Gu, *Analysis and comparison of medium voltage high power DC/DC converters for offshore wind energy systems*. IEEE Trans. Power Electron., vol. 28, no. 4, pp. 2014 – 2023, 2013.
- [5] D. Duij, F. Kieferndorf, and F. Canales, *Power electronic transformer technology for traction applications-An overview*. Proc. 7th. Int. Pow. Electron. Mot.Contr. (PEMC), vol. 16, no. 1, pp. 5056, 2012.
- [6] M. Steiner and H. Reinold, *Medium frequency topology in railway applications*. Eur. Conf. Power Electron. Appl. EPE, 2007.
- [7] H. Hoffmann and B. Piepenbreier, *Medium frequency transformer in resonant switching dc/dc-converters for railway applications*. Proc. 2011 14th Eur. Conf. Power Electron. Appl., pp. 1–8, 2011.
- [8] L. Heinemann, *An actively cooled high power, high frequency transformer with highinsulation capability*. APEC. Seventeenth Annu. IEEE Appl. Power Electron. Conf. Expo., vol. 1, no. c, 2002.
- [9] J. W. Kolar and G. I. Ortiz, *Solid State Transformer Concepts in Traction and Smart Grid Applications Schedule / Outline*. EPE-PEMC, pp. 1–166, 2012.
- [10] G. I. Ortiz, *High-Power DC-DC Converter Technologies for Smart Grid and Traction Applications*. Ph.D. dissertation, Inst.Pow.Electr.Driv., ETH Zurich, 2014.
- [11] J. E. Huber and J. W. Kolar, *Analysis and design of fixed voltage transfer ratio DC/DC converter cells for phase-modular solid-state transformers*. IEEE Energy Convers. Congr. Expo. ECCE 2015, pp. 5021–5029, 2015.
- [12] D. Rothmund, J. E. Huber, and J. W. Kolar, *Operating behaviour and design of the half-cycle discontinuous-conduction-mode series-resonant-converter with small DC link capacitors*. IEEE 14th Work.on Ctrl. and Mod. of Power Electronics, pp. 19, 2013.
- [13] M. Hergt, D. Kurthakoti and C. Schacherere, *Connecting power plants to high voltage networks*. U.S. Patent 0 149 509, May 26, 2016.
- [14] V. Vorperian and S. Cuk, *A complete DC analysis of the series resonant converter*. IEEE Power Electronics Specialists conference, pp. 85-100, 1982.
- [15] R. W. Erickson, *Fundamentals of Power Electronics, Second edition*.
- [16] F. Wittulski and R. W. Erickson, *Steady-State Analysis of the Series Resonant Converter*. IEEE Trans. Aerosp. Electron. Syst., vol. AES-21, no. 6, pp. 791–799, 1985.
- [17] C. G. Dincan and P. C. Kjaer, *DC-DC Converter and DC-DC conversion method*. Patent application, no. 70059, 2017.
- [18] J. Jacobs, A. Averberg, and R. De Doncker, *A novel three phase series resonant converter for high power Applications*. 35th Annual Power Electronics Specialists Conference, pp. 1861–1867, 2004.
- [19] G. Ortiz, D. Bortis, J. W. Kolar, and O. Apeldoorn, *Soft-switching techniques for medium-voltage isolated bidirectional DC/DC converters in solid state transformers*. IECON Proc. (Industrial Electron. Conf.), no. Iecon, pp. 5233–5240, 2012.
- [20] Fu-sheng Tsai, Peter Materu, Fred C.Y.Lee, *Constant-frequency clamped-mode resonant converters*. IEEE Transactions on Power Electronics, vol.3, no.4, october 1988.
- [21] Biju S. Nathan and V. Ramanarayanan, *Analysis, simulation and design of series resonant converter for high voltage applications*. Proceedings of IEEE International Conference on Industrial Technology, pp. 688-693, 2000
- [22] Fu-sheng Tsai, Fred C.Y.Lee, *A complete dc characterization of a constant-frequency, clamped-mode, series-resonant converter*. Power Electronics Specialists Conference, pp. 987–996, April 1988.
- [23] R. Lenke, J. Hu, R. W. De Doncker, *Unified Steady-State Description of Phase-Shift-Controlled ZVS-Operated Series-Resonant and Non-Resonant Single-Active-Bridge Converters*. IEEE Energy Conversion Congress and Exposition, pp. 796-803, September 2009.
- [24] Y. V. Singh, K. Viswanathan, R. Naik, J. A. Sabate, and R. Lai, *Analysis and control of phase-shifted series resonant converter operating in discontinuous mode*. Conf. Proc. - IEEE Appl. Power Electron. Conf. Expo. - APEC, pp. 2092–2097, 2013.
- [25] P. Ranstad, H. H.-P. H. Nee, and J. Linner, *A novel control strategy applied to the series loaded resonant converter*. Eur. Conf. Power Electron. Appl., pp. 1–10, 2005.
- [26] M. T. Daniel, H. S. Krishnamoorthy, P. N. Enjeti, *A new wind turbine interface to MVDC collection grid with High frequency isolation and input current shapin*. IEEE Journal of Emerg. and Selec. Top. in Pow.Elec., vol. 3, no. 4, pp. 967-976, 2015.
- [27] D. Jovcic, *Step-up DC-DC converter for megawatt size applications*. IET Power Electronics., vol. 2, no. 6, pp. 675685, 2009.
- [28] D. Jovcic, *Bidirectional, high-power DC-transformer*. IEEE Trans.Power Deliv., vol. 25, no. 4, pp. 2164-2173, 2010.
- [29] D. Dujic, A. Mester, T. Chaudhuri, A. Coccia, F. Canales, and J. K. Steinke, *Laboratory scale prototype of a power electronic transformer for traction applications*. Proc. 2011 14th Eur. Conf. Power Electron. Appl., vol. i, pp. 1–10, 2011.
- [30] G. Ortiz, H. Uemura, D. Bortis, S. Member, J. W. Kolar, and O. Apeldoorn, *Modeling of Soft-Switching Losses of IGBTs in DC / DC Converters*. vol. 60, no. 2, pp. 587–597, 2013.
- [31] L. Lindenmuller, R. Alvarez, P. Kleinichen, and S. Bernet, *Characterization of a 6.5 kV / 500A IGBT module in a series resonant converter*. vol. IEEE Energy Convers. Congr. Expo., pp. 4138 – 4143, 2011.
- [32] R. King and T. Stuart, *Transformer Induced Instability of the Series Resonant Converter*. IEEE Trans. Aerosp. Electron. Syst., vol. AES-19, no. 3, pp. 474–482, 1983.
- [33] H. Klessner and J. Klaassens, *Transformer-Induced Low-Frequency Oscillations in the Series-Resonant Converter*. IEEE Trans. Power. Electron., vol. 6, no. 3, pp. 326–337, 1991.
- [34] G. Ortiz, L. Fassler, J. Kolar and O. Apeldoorn, *Flux balancing of isolation transformers and application of "the magnetic ear" for closed loop volt second compensation*. IEEE Trans. Power. Electron., vol. 29, no. 8, pp. 4078–4090, 2014.



Catalin Dincan (S'17) received the B.Sc. degree in electrical engineering from the Technical University of Cluj-Napoca, Cluj-Napoca, Romania, in 2009, and the M.Sc. degree in power electronics and drives from Aalborg University, Aalborg, Denmark in 2011. After his studies he worked as a hardware engineer with Danfoss Solar Inverters until 2015, and currently he is working toward the Ph.D degree. His current research interests include the design of high power, medium voltage, resonant converters for offshore wind turbines.



Philip Kjaer (S'92-M'93-SM'11) received the M.Sc. degree in electrical engineering from Aalborg University, Aalborg, Denmark, in 1993, and the Ph.D. degree from the University of Glasgow, Glasgow, U.K., in 1997. From 1993 to 1998, he was a Research Assistant at the University of Glasgow, working with advanced control of switched reluctance machines and drives. From 1998 to 2003, he was with ABB Corporate Research, Vasteras, Sweden, where, as a Development Engineer, he worked on servo-motor-based high-voltage circuit

breaker drives, factory testing of synchronous machines, power converters for HVDC power transmission, and multi-megawatt variable-speed drives. In 2003, he joined Vestas Wind Systems, Arhus, Denmark, where he holds the position as Chief Specialist for Electrical Power Technology. Since 2013, he has been associated part-time professor with Aalborg University. His research covers control and application of power electronic converters, and he has 100 journal and conference publications and more than 20 patents in this field. Dr. Kjaer is a Chartered Engineer in the U.K., a Member of the Institution of Electrical Engineers, U.K., member of FEANI, member of the Danish Academy of Technical Sciences, member of the Danish national committee of Cigr, and the recipient of the 2004 Richard M. Bass Outstanding Young Power Electronics Engineer Award.



Yu-hsing Chen was born in Kaohsiung, Taiwan, on December 12, 1979. He received the B.S. degree from Kun Shan University, Tainan, Taiwan, in 2002 and the M.S. and Ph.D. degrees from National Tsing Hua University, Hsinchu, Taiwan, in 2004 and 2010, respectively. His research interests include voltage sag ride-through technologies and converter controls.



Stig Munk-Nielsen (S'92-M'97) received the M.Sc. and Ph.D. degrees from Aalborg University, Aalborg, Denmark, in 1991 and 1997, respectively. He is currently Professor WSR at the Department of Energy Technology, Aalborg University. His research interests include LV and MV converters, packaging of power electronic devices, electrical monitoring apparatus for devices, failure modes and device test systems. In the last ten years, he has been involved or has managed 10 research projects, including national and European Commission projects.



Claus Leth Bak (M'1999, SM'2007) received the B.Sc. with honors in Electrical Power Engineering in 1992 and the M.Sc. in Electrical Power Engineering at the Department of Energy Technology (ET) at Aalborg University (AAU), Denmark in 1994. After his studies he worked as a professional engineer with Electric Power Transmission and Substations with specializations within the area of Power System Protection at the NV Net TSO. In 1999 he was employed as an Assistant Professor at ET-AAU, where he holds a Full Professor position today. He received the PhD degree in 2015 with the thesis EHV/HV underground cables in the transmission system. He has supervised/co-supervised +35 PhDs and +50 MSc theses. His main Research areas include Corona Phenomena on Overhead Lines, Power System Modeling and Transient Simulations, Underground Cable transmission, Power System Harmonics, Power System Protection and HVDC-VSC Offshore Transmission Networks. He is the author/coauthor of app. 250 publications. He is a member of Cigr JWG C4-B4.38, Cigr SC C4 and SC B5 study committees member and Danish Cigr National Committee. He received the DPSP 2014 best paper award and the PEDG 2016 best paper award. He serves as Head of the Energy Technology PhD program (+ 100 PhDs) and as Head of the Section of Electric Power Systems and High Voltage in AAU and is a member of the PhD board at the Faculty of Engineering and Science.